Electronic Digital Materials

by

William Kai Langford

B.S., Tufts University (2012)

Submitted to the Program in Media Arts and Sciences,
School of Architecture and Planning
in partial fulfillment of the requirements for the degree of

Master of Science

at the

MASSACHUSETTS INSTITUTE OF TECHNOLOGY

September 2014

© Massachusetts Institute of Technology 2014. All rights reserved.

Author . . . .
Program in Media Arts and Sciences,
School of Architecture and Planning
August 18, 2014

Certified by . . . .
Neil A. Gershenfeld
Director, Center for Bits and Atoms
Thesis Supervisor

Accepted by . . . .
Prof. Pattie Maes
Interim Academic Head, Program in Media Arts and Sciences

Electronic Digital Materials

by

William Kai Langford

Submitted to the Program in Media Arts and Sciences,
School of Architecture and Planning
on August 18, 2014, in partial fulfillment of the
requirements for the degree of
Master of Science

Abstract

Digital materials are constructions assembled from a small number of types of discrete building blocks; they represent a new way of building functional, multi-material, three-dimensional structures. In this thesis, I focus on the construction of microelectronics from vertically assemble-able two-dimensional parts. With just a conducting and insulating part-type, I show that it is possible to make discretely assembled electrical networks. With a third resistive part-type, I show that it is possible to make any passive electronic component and complex impedance circuitry, including antennas and matching networks. Finally, with four semiconducting part-types I suggest that it is possible to assemble active components like diodes and transistors. This work details the part production processes to create two-dimensional micro-bricks, modeling and assembly strategies to create functional structures from discrete parts, the measurement and evaluation of the bulk properties of the assemblies, and experiments in assembly automation.

Thesis Supervisor: Neil A. Gershenfeld
Title: Director, Center for Bits and Atoms

Electronic Digital Materials

by

William Kai Langford

The following people served as readers for this thesis:

Professor Joseph A. Paradiso . . . .
Associate Professor of Media Arts and Sciences
Director, Responsive Environments

Professor Jennifer A. Lewis . . . .
Hansjörg Wyss Professor of Biologically Inspired Engineering,
Harvard School of Engineering and Applied Sciences

Acknowledgments

First and foremost, I would like to thank Neil Gershenfeld for creating the Center for Bits and Atoms; it is a unique and amazing place to work in and I'm continually inspired by the people it attracts. I also want to thank Neil for continually pushing me to do things I don't believe I am capable of; this is a force I want to keep with me for the rest of my life.

I would also like to thank my readers, Jennifer Lewis and Joe Paradiso, for taking time out of their busy schedules to meet with me and offer their insights on my work.

This work could not have been accomplished if it wasn't for the people that keep CBA running like a well-oiled machine: Joe and Ryan for making purchasing so easy and painless, Theresa and Jamie for always being so helpful and accommodating with last minute requests, and of course, John and Tom for making the shop a safe place to play.

Finally, I would like to thank my friends and family for their constant support and encouragement. In particular, I'd like to thank Carlos and Sam for their friendship—both outside and inside the lab; your work continually inspires me and pushes me to better my own.

Contents

1 Introduction **19**

1.1 Background . . . 19

1.2 Related Work . . . 20

2 Part Design and Fabrication **23**

2.0.1 Insulator . . . 23

2.0.2 Conductor . . . 24

2.0.3 Resistor . . . 25

2.0.4 Semiconductors . . . 27

2.1 Geometry . . . 28

2.1.1 Design Decisions . . . 28

2.1.2 Part Design Enhancements . . . 29

2.2 Fabrication . . . 31

2.2.1 Insulating and Resistive Parts . . . 31

2.2.2 Conductive Parts . . . 33

2.2.3 Semiconducting Parts . . . 35

3 Discretely Assembled Circuits **41**

3.1 Three-Dimensional Electrical Networks . . . 41

3.1.1 Design . . . 42

3.1.2 Assembly . . . 43

4 Discretely Assembled Passive Components **45**

4.1 Analysis . . . 46
    4.1.1 Capacitors . . . 46
    4.1.2 Inductors . . . 47
    4.1.3 LC Resonators . . . 48
4.2 Assembly . . . 49
4.3 Evaluation . . . 52
    4.3.1 LCR Meter . . . 52
    4.3.2 Frequency Response Analysis . . . 54

5 Discretely Assembled Active Components 61
5.1 Analysis . . . 61
    5.1.1 Schottky Diode . . . 61
    5.1.2 MOSFET . . . 63
5.2 Assembly . . . 64
5.3 Evaluation . . . 66

6 Simulation 69
6.1 COMSOL Modeling . . . 69
6.2 FDTD Solver . . . 71

7 Evaluation and Measurement 75
7.1 Contact Resistance . . . 75
7.2 Reversibility . . . 77
7.3 Response to Load of a Single Joint . . . 79
7.4 Bulk Response to Load . . . 81
7.5 Bulk Temperature Dependence . . . 85
7.6 Surface Roughness of Contacting Surfaces . . . 89
7.7 Implications for Reducing Contact Resistance . . . 90

8 Scaling 93
    8.0.1 Part Fabrication . . . 93
    8.0.2 Capacitors . . . 94

8.0.3 Integrated Circuits 96

9 Assemblers 97

9.1 Discrete Relative-Motion Assemblers 98

9.1.1 Parallel assembly 98

9.1.2 Serial assembly 100

10 Conclusion 105

List of Figures

1-1 Previous work done on digital micro-assembly in the Center for Bits and Atoms. 20
1-2 Previous work done on digital micro-assembly in the Cornell Creative Machines Lab. 21

2-1 Insulating parts made from various materials: (left to right) fishpaper, polyester, polyimide, Garolite. 24
2-2 Three parts made from different resistive materials: (left to right) static-dissipative ultra high molecular weight polyethylene, 0-90-0 unidirectional carbon fiber layup, woven carbon fiber 26
2-3 Dimensioned drawing of part 28
2-4 Potential scraping/wiping contact slot design. 29
2-5 Snap-fit part geometry experiments 30
2-6 Hierarchy can be achieved through the use of adapter parts. 30
2-7 Assembly of milled polyester parts 31
2-8 Custom punch press used to stamp parts 32
2-9 Punch press close up 33
2-10 Brass parts milled on the Hurco 34
2-11 Brass shim stock sheets sandwiched between aluminum plates 35
2-12 Excimer cut part next to brass part produced using the Wire-EDM. . 36
2-13 Dicing a silicon wafer in the Hurco VM10U. 37
2-14 Close up of result of silicon wafer after dicing. Cracking is in the ⟨001⟩ > direction. 37

2-15 Showing close up of edge created by dicing saw. Some chipping is evident. 38
2-16 Fixture used to cut slots in the parts 38
2-17 A SEM micrograph of the slot of a part made with the DPSS laser from Oxford Lasers, Inc. [1] 39
2-18 A slot made with the microwaterjet (left) compared with one from the dpss laser (right) 40
2-19 High aspect-ratio gears made with DRIE. [33] 40

3-1 The two part types needed to make an arbitrary 3D circuit. 41
3-2 Discretely assembled circuit render. 42
3-3 The top few layers of the design of a discretely assembled circuit. . . . 43
3-4 Discretely assembled circuit board blinks an LED on and off. 43

4-1 A diagram of a discretely assembled interdigitated capacitor (top-down view). 46
4-2 A discretely assembled inductor (middle) and capacitor (right) next to a penny for scale. 49
4-3 Assembling a discrete capacitor 50
4-4 An epoxy substrate serves as an electrically insulating substrate. . . . 51
4-5 A family of discretely assembled capacitors 51
4-6 A discretely assembled inductor with an x-ray view of the interior. . . 52
4-7 A discrete resistor asssembled from anti-static polymer parts. 52
4-8 A plot showing how capacitance scales linearly with the number of conductive parts assembled. 53
4-9 The RC circuit used to measure the frequency response of the capacitor. 55
4-10 A bode plot showing amplitude and phase shift of a capacitor. 56
4-11 The RL circuit used to measure the frequency response of the inductor. 56
4-12 A bode plot showing amplitude and phase shift of a inductor. 57
4-13 The RLC circuit used to measure the frequency response of the LC Resonator. 57
4-14 A bode plot showing amplitude and phase shift of an LC resonator. . 58

4-15 Q-Factor analysis of the LC Resonator. 59

5-1 A simulation of a diode made with copper and aluminum. 63
5-2 A schematic render of how a MOSFET could be discretely assembled. 64
5-3 Two Schottky diode assemblies: a successful press-fit connection (left), a failed press-fit part insertion (right). 65
5-4 The clamped diode's construction. 66
5-5 The clamped diode's IV characteristics. 67

6-1 Modeling a single inductor loop and interdigitated parallel plates . . . 70
6-2 COMSOL modeling of small inductor assemblies. The single spiral inductor (left) has an inductance of 5.1 nH while the two spiral inductor (right) has an indutance of 13.9 nH 70
6-3 Electromagnetic modeling of LC resonator. 71
6-4 FDTD solver validation 72
6-5 FDTD simulation of a micro-patch antenna. 72
6-6 FDTD simulation of a spiral chip antenna. 73

7-1 Actual contact area restricts current flow through asperities. [37] . . . 76
7-2 Industrial Press-Fit Connection [18] 77
7-3 Joint cycling machine 77
7-4 Joint cycling machine 78
7-5 Resistance of joint vs number of cycles 79
7-6 Instron measurement test setup 79
7-7 Conductance and load vs displacement (left). Resistance of joint with applied compressive load (right). 80
7-8 Bulk resistance test specimen. 81
7-9 Bulk resistance fixture block. 82
7-10 Bulk resistance test specimen in instron. 82
7-11 Time series of conductance, load, and displacement over 20 cycles. . . 83

7-12 Plot of conductance/extension and load/extension loops over 20 cycles. The red circle denotes the start of the experiment and the red diagonal denotes the end. 84
7-13 Plot of change in extension and conductance over 20 cycles. 85
7-14 Temperature response fixture 86
7-15 Time series showing conductance, load, and temperature over four cycles. 87
7-16 Plot of conductance over four temperature cycles. 88
7-17 SEM micrograph of a part in an assembly. 89
7-18 SEM micrograph of a slot that has not been used. 90
7-19 SEM micrograph of a slot that has been used. 90

8-1 A number of parts made at various scales with feature sizes ranging from 0.25 inches to 100 µm 93
8-2 A QFN pitch part made via wire-edm shown with a human hair for scale (left). Another QFN pitch part made via excimer laser micromachining (right). 94
8-3 A plot showing how capacitance per volume increases with decreasing lattice pitch. 95

9-1 Parts are sequentially loaded into the rows of the pin array from the edge. 98
9-2 Experimental demonstration of parallel assembly technique. 99
9-3 Failure modes of the parallel assembly technique. 100
9-4 A render of a stapler assembler. 101
9-5 A diagram showing the parts of a stapler assembler. 101
9-6 Rotary cam mechanism to produce discrete steps from continuous rotation. 102
9-7 A prototype of a stapler-style assembler. 102
9-8 The stapler assembler in use. 103

List of Tables

2.1 A comparison of metals to be used as a conductive part-type. 25

9.1 Table showing how part deposition rate scales with characteristic part size. 97

Chapter 1

Introduction

1.1 Background

There has been recent academic and commercial interest in additive manufacturing for its ability to create complex three-dimensional structures. The forefront of this research looks to enable the fabrication of objects from multiple materials in order to embed functionality within physical structures. However, the material constraints imposed by conventional additive manufacturing processes (e.g., thermoplastics, UV-cure photopolymers, and metal powders) make true multi-material objects very difficult to achieve in practice. [21] This work, instead, builds on recent research which looks to digitize fabrication; this means assembling structures from discrete parts rather than depositing or removing material.

In a digitally assembled structure, discrete parts interlock with neighboring ones such that they register to a lattice and have a discrete set of possible positions and orientations. The connections between parts are made with reversible, mechanical snap-fit or press-fit connections. The function of these is akin to a chemical bond in which some activation energy is needed to overcome the energy barrier of adding or removing a part. These traits enable the assembly of precise structures with imprecise tools (imagine a young child building a micron-precise Lego structure). [26]

Digital assembly lends itself very well to creating functional multi-material structures; they are simply assembled from multiple types of parts, each with a different functional property (e.g., conductive, insulating, rigid, flexible, etc...). By making each part-type a single material, an assembly can leverage the bulk properties of its constituent parts.

This work focuses on the discrete assembly of functional multi-material structures and specifically looks to show that three-dimensional microelectronics can be assembled from simple press-fit parts. I show that it is possible to assemble electrical interconnect, passive components, and active components from less than ten unique part-types. I also evaluate the assembled structures, looking at both the bulk electrical properties of the structure as well as the properties at the interfaces between parts.

1.2 Related Work

My research group, the Center for Bits and Atoms, has done previous work in characterizing digital materials at many length-scales and for various applications. George Popescu characterized the tunability of multi-material digitally assembled structures, assembled a press-fit diode, and sketched a vision for an automated assembler. [26] Jonathan Ward developed a more concrete representation of how an automated assembler would function and furthermore how an automated assembler may itself be made of a digital material. [34]

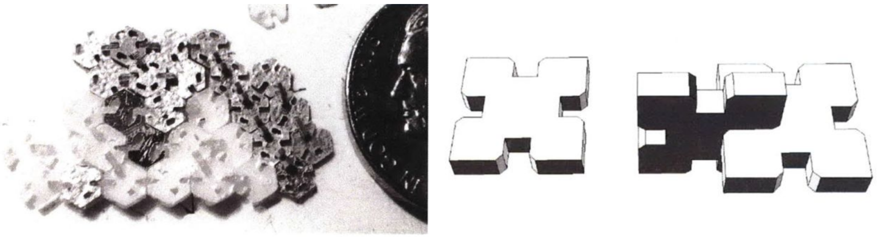

(a) A press-fit assembly created by Jonathan Ward [34]

(b) The press-fit part geometry employed by George Popescu [26]

Figure 1-1: Previous work done on digital micro-assembly in the Center for Bits and Atoms.

The Creative Machines Lab at Cornell University, headed by Hod Lipson, has explored similar research in creating functional multi-material structures with digital materials. In “Methods of Parallel Voxel Manipulation for 3D Digital Printing,” Hiller and Lipson demonstrate a machine that is capable of placing spheres of material to construct objects. The assembler is capable of building multi-material structures from polymer and metal parts. [15]

More recently, MacCurdy et al. showed discrete assembly of electrical circuits using “BitBlox” in which small circuit boards, each with a different function (e.g., LED, microcontroller, battery), are vertically assembled with press-fit connections to create functional circuitry. [22]

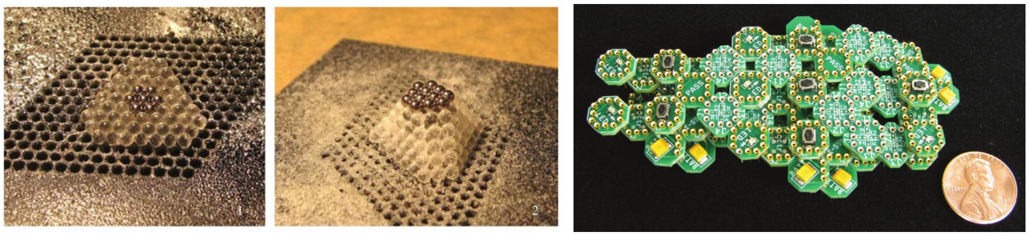

(a) A voxel printer that assembles objects from spheres of various materials [16]

(b) More recently MacCurdy et al. created an electronic digital materials called BitBlox [22]

Figure 1-2: Previous work done on digital micro-assembly in the Cornell Creative Machines Lab.

In “Design and Analysis of Digital Materials for Physical 3D Voxel Printing,” Hiller and Lipson present a relatively thorough comparison of different kinds of digital material and compare them across a number of traits including the part’s ability to self-align, its manufacturability, and how it fills space. [16] MacCurdy et al. present a similar table comparing 25 potential digital material implementations with a focus on module size and complexity as well as the electrical connectivity and actuation present in the materials. [22]

Chapter 2

Part Design and Fabrication

In order to fabricate functional microelectronics, a number of different materials are necessary. An insulator is needed to isolate electrical pathways, a conductor is needed to carry current, a resistive material is needed to impede current, and semiconductors are needed to produce nonlinear devices with power gain.

To digitize the fabrication of electronics, it is necessary to define a basis set of part-types from which all electronic functionality can be assembled. Digital assembly provides a unique framework for combining different materials, and therefore, enables each part-type to consist of a single bulk material. Given this, I have worked to select a material for each part-type that will enable the construction of high-performance multi-material electronic structures. This section details the decision processes that led to the selection of each material part-type.

2.0.1 Insulator

In choosing an insulating material, I considered a number of different factors, including elastic modulus, dielectric strength, and temperature stability.

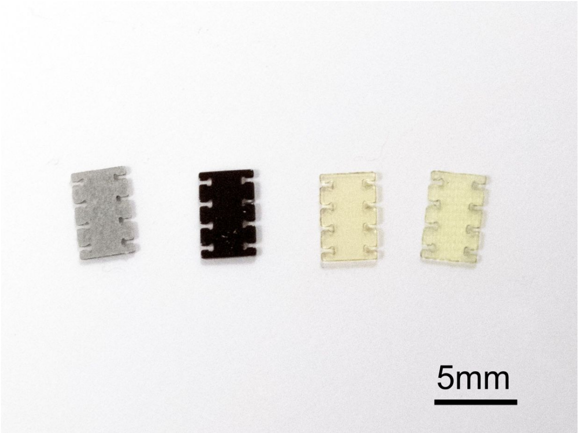

Figure 2-1: Insulating parts made from various materials: (left to right) fishpaper, polyester, polyimide, Garolite.

Initially I chose to use polyester precision shim stock for its precision thickness tolerance, ready availability, and ease of machining. I eventually switched to a Garolite fiber-epoxy composite for improved stiffness and strength, as well as better temperature and humidity stability. It is also already widely used in conventional printed circuit board substrates.

2.0.2 Conductor

In choosing a material to make the conductive parts with, one needs to balance the mechanical stability and electrical conductance of joints in the resulting assembly, while also acknowledging fabrication and supply chain related constraints.

In comparing the materials, I compiled Table 2.1 to evaluate the strengths and weaknesses of candidate metals across a few important traits including stiffness, strength, hardness, and resistivity.

Material	Resistivity (Ω*m)	Elastic Modulus (GPa)	Strength (UTS) (MPa)	Hardness (Brinell)
Copper	1.7×10^{-8}	124	220	35
Aluminum (pure)	2.7×10^{-8}	68	70	15
Aluminum (6061)	3.9×10^{-8}	69	310	95
Brass	5.9×10^{-8}	100	250	65
Steel (mild)	15×10^{-8}	200	400	130

Table 2.1: Table values sourced from: [4][5]

Copper is a relatively soft, ductile metal with very high conductivity, and for this reason is the most common metal used in electronic interconnect. [27] While the softness of copper makes it well suited for many electronic contact and interconnect applications, it also makes it difficult to machine.

Brass is an alloy composed of copper and zinc. It maintains relatively high electrical conductivity, but is considerably easier to machine than copper. For this reason, I have chosen to use brass as the conductor for the majority of the assemblies presented in this work.

While brass may be well suited for prototyping electronic digital material assemblies, other materials may need to be explored in order to push the performance limits of this fabrication strategy. These alternatives are explored further in Section 7.7.

2.0.3 Resistor

To make discretely assembled resistors we need a resistive part type.

Commercial resistors are made from a variety of different materials. The highest precision resistors are made from a very thin ($\approx 500\,\text{Å}$) metal films. [32] Lower quality resistors can be made from carbon-ceramic mixture or from resistive films (e.g., tin oxide). [3]

To enable the construction of a wide range of resistances, an individual resistive part should have a resistance that lies approximately in the middle of the desired range of resistances. This allows parts to be combined in parallel to reach small resistance values and in series to achieve large resistance values.

The resistance of each part can be expressed with the following equation in which ρ is the bulk resistivity of the material (with units of $\Omega\,\mathrm{cm}$) and l, w, and t are a measure of the part's length, width, and thickness respectively.

$$R = \frac{\rho l}{A} = \frac{\rho l}{wt} = \left(\frac{\rho}{t}\right)\left(\frac{l}{w}\right) = R_s\left(\frac{l}{w}\right) \tag{2.1}$$

Here, R_s has units of $\Omega/\square$ and is a measure of surface resistivity. This parameter can be directly measured using a two-point or four-point measurement scheme and provides a good means of estimating the resistance of a part with uniform thickness. [35]

Electrostatic dissipative materials are materials that are designed to leak charge and reduce the buildup of static electricity. They have sheet resistances that lie between that of insulators and conductors. Static-dissipative polymers, for example, have sheet resistances that lie roughly between 10^6 and 10^9 $\Omega/\square$. [7]

Carbon can also serve as a resistive material and may be processed into parts in a number of different ways. Figure 2-2 shows a carbon fiber part made by laying up three layers of unidirectional pre-preg fiber in a 0-90-0 configuration and one made from a woven fiber sheet. Graphite powder may also be used as an additive in a molding and casting process to make, for example, conductive epoxy parts. [24] This process has the added benefit that the resistivity of the part can, to some degree, be controlled by the amount of graphite powder that is added to the matrix.

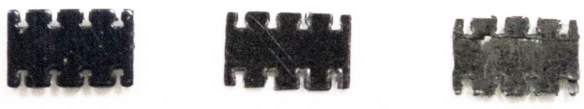

Figure 2-2: Three parts made from different resistive materials: (left to right) static-dissipative ultra high molecular weight polyethylene, 0-90-0 unidirectional carbon fiber layup, woven carbon fiber

Ultimately I decided to use the static dissipative plastic. Individual part resistances were found to be approximately $100\,\mathrm{k\Omega}$ which enables the creation of resistor assemblies with values ranging from $100\,\Omega$ to $100\,\mathrm{M\Omega}$ with fewer than 1000 parts.

2.0.4 Semiconductors

In order to make active electronics like diodes and transistors, semiconducting parts are necessary.

There are a number of different types of semiconducting materials, but monocrystalline silicon is by far the most commonly used material in the integrated circuits industry for its electrical and temperature stability. [38]. By doping the silicon with impurities, its conductivity and electrical behavior can be controlled.

In order to to make an NP diode, an N-type MOSFET, and a P-type MOSFET, we need four types of semiconducting parts: N-doped silicon, P-doped silicon, highly doped N-type silicon (N+), and highly-doped P-type silicon (P+).

Highly doped silicon commonly has a resistivity on the order of $10\,\mathrm{m\Omega\,cm}$. In this case, I am using wafers with a resistivity between $1\,\mathrm{m\Omega\,cm}$ and $5\,\mathrm{m\Omega\,cm}$ which corresponds to a dopant concentration of approximately $1 \times 10^{19}\,\mathrm{cm^{-3}}$ for phosphorous doped N-type wafers and $1 \times 10^{20}\,\mathrm{cm^{-3}}$ for boron doped P-type wafers.

In contrast, standard doped silicon has a resistivity on the order of $10\,\Omega\,\mathrm{cm}$. In this case, the wafers I am using have a resistivity of $1\,\Omega\,\mathrm{cm}$ to $10\,\Omega\,\mathrm{cm}$ which corresponds to a dopant concentration of approximately $1 \times 10^{15}\,\mathrm{cm^{-3}}$ for phosphorous doped N-type wafers and $1 \times 10^{16}\,\mathrm{cm^{-3}}$ for boron doped P-type wafers.

In addition to these semiconducting materials, a Schottky diode requires metals with particular work functions. In this work, I use copper ($4.7\,\mathrm{eV}$) and aluminum ($4.08\,\mathrm{eV}$) to create a rectifying and an ohmic contact, respectively. While these materials do not provide optimal performance for Schottky and ohmic contacts, they are readily available and far easier to work with than more conventionally used materials like gold, tungsten, and platinum.

2.1 Geometry

2.1.1 Design Decisions

The parts look the way they do for a number of reasons. First, they are two dimensional and the geometry is as simple as possible. This makes fabrication across many length-scales and with many different materials possible. Second, they are vertically assemble-able. The slots on the top and bottom allow the structures to be assembled one part at a time, in a vertical fashion. Additionally, the number of slots on the top and bottom are the minimum needed to tile the parts orthogonally while still maintaining the structural integrity of the assembly as a whole. Finally, the part thickness with respect to lattice pitch was chosen to be a good compromise between mechanical stiffness of the individual joint and the density of the whole assembly.

I fabricated the parts at two scales: one with feature sizes of 0.010 in with a lattice pitch of 0.05 in and one with feature sizes of 0.020 in with a lattice pitch of 0.1 in . The larger scale parts were necessary in order to accommodate standard silicon wafer thicknesses (500 µm) and the fabrication constraints of the tools able to process silicon. The smaller parts are scaled such that the assembled lattice has a pitch that matches the lead spacing of SOIC surface mount components (0.05 in). This enables the assembly of three-dimensional circuit boards that use conventional components.

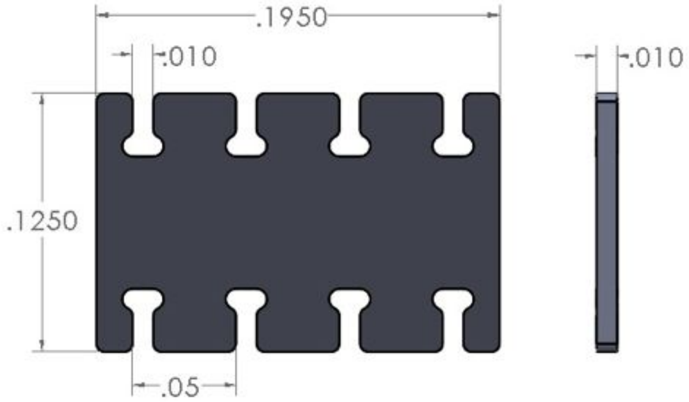

Figure 2-3: Dimensioned drawing of part

2.1.2 Part Design Enhancements

Flexural electrical contact

The performance of the digital materials may be enhanced with more complex part geometries. For example, flexural electrical contacts could be integrated into the slots to further reduce electrical contact resistance between parts. This could include a wiper or scraper that helps to remove contamination such as oxide layers during the press-fit assembly. This topic of sprung electrical contacts is well studied and provides design guidelines for further enhancements. [28], [12]

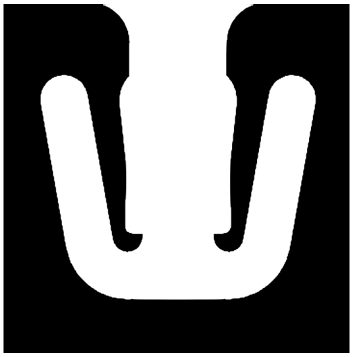

Figure 2-4: Potential scraping/wiping contact slot design.

Snap-fit

Geometry could also be added to increase mechanical stiffness in certain directions. For example, while the simple slotted press-fit cannot withstand large tensile loads, by adding snap-fit geometries, larger tensile loads can be tolerated. Pictured below are snap-fit geometries I explored at a larger scale. By tuning the angle of the chamfer on the flexural elements it is possible to tune the relative bias between the force required to install and remove the part.

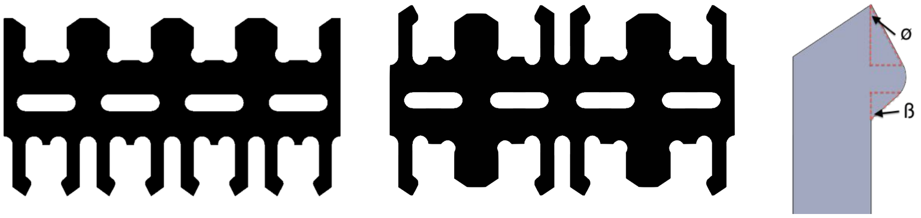

(a) Figure A (b) Figure B (c) Figure C

Figure 2-5: Snap-fit part geometry experiments

Hierarchy

With the addition of two part-types, the parts can be made to be hierarchical. That is to say, it is possible to join assembled lattices of different length-scales through the use of special adapter parts. Figure 2-6 shows 0.020 in thick aluminum parts that are joined with 0.010 in thick brass parts.

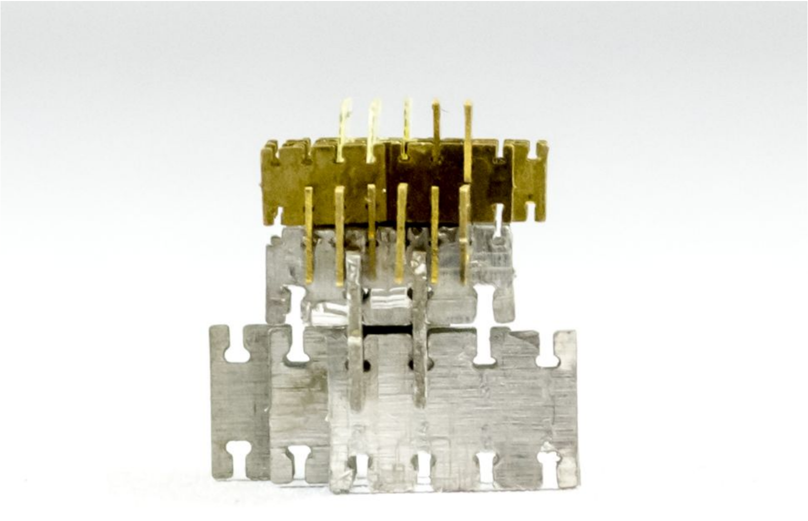

Figure 2-6: Hierarchy can be achieved through the use of adapter parts.

2.2 Fabrication

2.2.1 Insulating and Resistive Parts

For prototyping, the insulating and resistive parts were milled out of 0.01 in plastic shim stock on the Shopbot Desktop CNC router using a 0.01 in endmill. Each part took roughly 3 minutes to make.

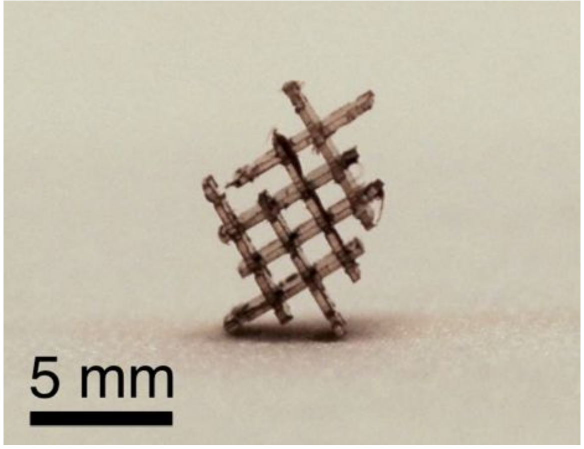

Figure 2-7: Assembly of milled polyester parts

In order to more rapidly produce parts, I developed a punch press that uses a custom tool and die to stamp out parts from strips of material (Figure 2-8). The tool and die are made from high strength corrosion resistant 17-4 stainless steel and were cut on the wire-EDM. The gap between the punch and die was designed to be 25.4 µm, or 10% of the material thickness, following standard tool and die guidelines. [11]

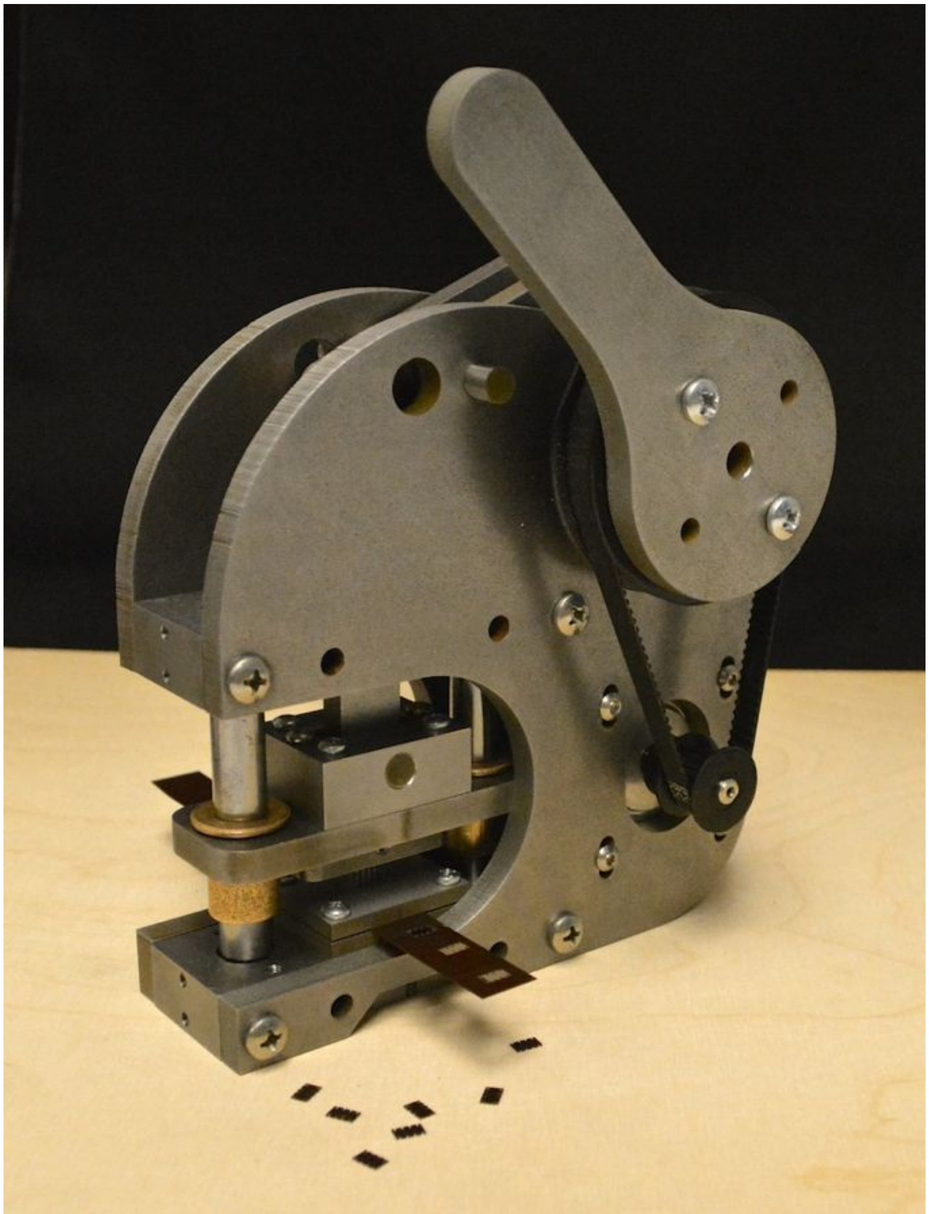

Figure 2-8: Custom punch press used to stamp parts

The linkage and punch press itself are made entirely from mild steel and are designed to amplify torque on the handle by approximately nine-times to produce upwards of 1 kN of force on the punch when operated by hand. The force required to punch out a part can be approximated using the equation:

$$F = \tau p t \tag{2.2}$$

where τ is the shear strength of the material, p is the perimeter of the geometry to be punched, and t is the material thickness.

For polyethylene this is: 33 MPa × 28 mm × 0.254 mm = 234.7 N

For Garolite (G-10/FR4) this is: 152 MPa × 28 mm × 0.254 mm = 1.081 kN

For brass this is: 344 MPa × 28 mm × 0.254 mm = 2.447 kN

Therefore, the nominal 1 kN of force is roughly what is required to punch 5 mm × 2 mm parts out of 254 µm garolite fiberglass. Brass on the other hand, requires more than two times the nominal amount of force the punch press can currently produce. However, this could be achieved by simply extending the lever arm of the handle and should be well within stress limits of the punch press.

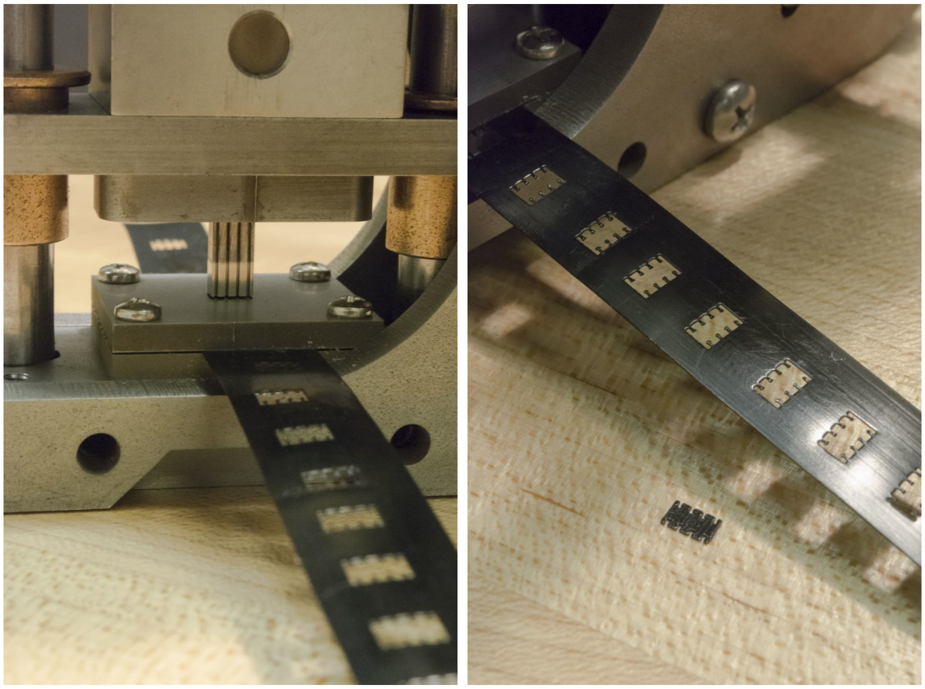

(a) Figure A

(b) Figure B

Figure 2-9: Punch press close up

2.2.2 Conductive Parts

The conductive parts were prototyped on the Hurco VM10U 5-axis CNC vertical machining center from 0.01 in precision brass shim stock using a 0.01 in endmill. The Hurco CNC's sturdy build and low-runout spindle made endmill breakage a far less common occurrence than it would have been using a machine like the Shopbot Desktop. Each part took roughly 12 minutes to machine since a very shallow ramping plunge was required in order to avoid breaking the endmill.

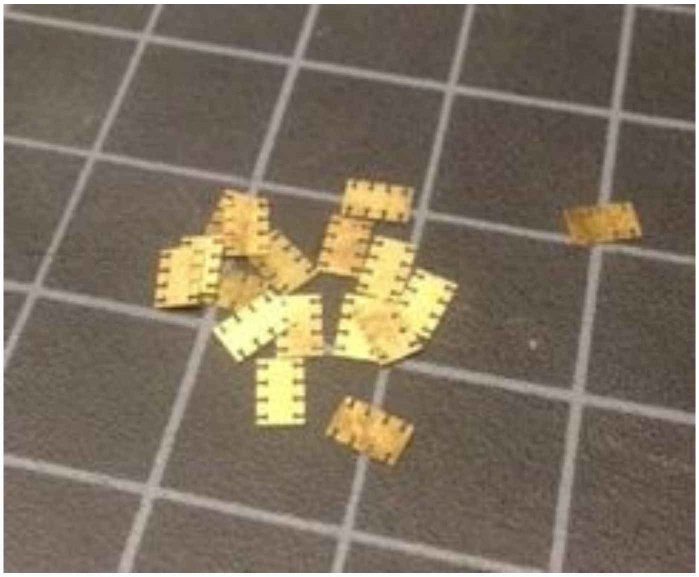

Figure 2-10: Brass parts milled on the Hurco

In order to speed up production (and given the availability of new tools), I produced the conductive parts in mass using a wire-cut EDM. The wire EDM works via a process called spark erosion, in which a thin brass wire (in this case 0.006 in diameter) is electrified and brought close to a conductive workpiece submerged in deionized water. The dielectric breakdown of the fluid in the gap between the wire and workpiece creates a spark which erodes material from the workpiece. [10]

Many parts can be fabricated at once by stacking thin sheets together and cutting the stack. Figure 2-11 shows the sandwiching fixture used to cut the majority of brass parts in this work. Two aluminum plates sandwich the thin brass sheets and countersunk screws keep the stack tightly held together.

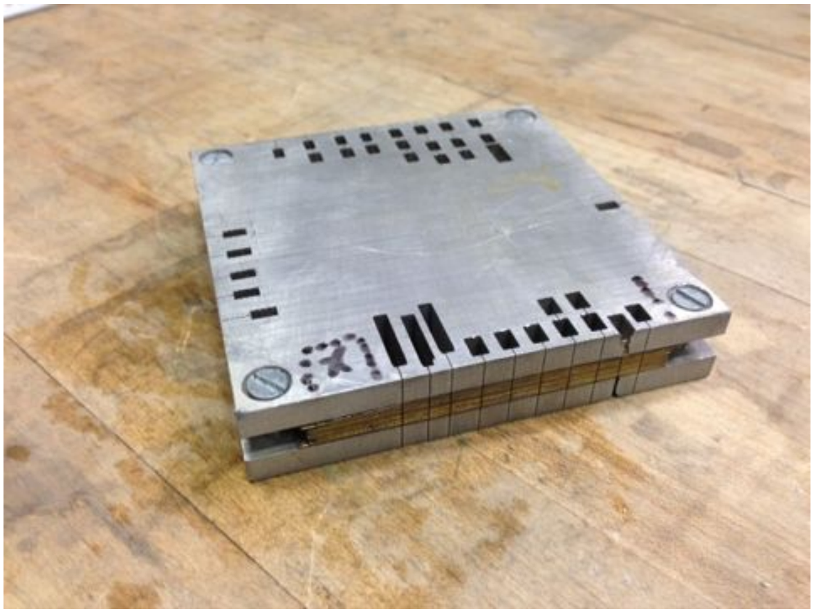

Figure 2-11: Brass shim stock sheets sandwiched between aluminum plates

2.2.3 Semiconducting Parts

Silicon is a brittle material and therefore cannot be machined the same way plastic or metal parts may be. Silicon wafers are conventionally scored or diced using mechanical scribes, lasers, and diamond dicing saws. [13] These techniques, however, are unable to produce the intricate geometry necessary to make a press-fit part.

This section details my experience producing silicon parts with various non-conventional fabrication techniques including my failed attempts with a wire-EDM, an excimer laser, and a diamond dicing saw, as well as my successes with a solid-state laser and micro-waterjet.

Wire-EDM

Heavily doped silicon (with volume resistivity on the order of $1\,\text{m}\Omega\,\text{cm}$) may, in theory, be cut using the wire-edm. [10][36] In practice, however, I found this often resulted in fracture of the silicon along its grain orientation.

Excimer Micromachining Laser

Excimer lasers (or excited dimer lasers) are often used to pattern features onto wafers for use in applications such as microfluidics and micromachining. We operate our excimer laser with a KrF gas mix which produces a 248 nm wavelength beam. Rather than a Gaussian beam, the excimer laser produces a flat-bottom beam, which makes them extremely useful for routing channels and achieving relatively straight side walls. While excimer lasers excel at surface micromachining, they are not particularly well-suited to bulk micromachining. By using the laser with very high de-magnifications (25x), it is possible bulk micro-machine 500 µm silicon but debris build-up, taper, and recast material become serious issues in achieving precise cuts with this depth of cut. Figure 2-12 shows a representative result of bulk machining silicon with the excimer. It is clear that the heat affected zone becomes a serious problem with this depth of cut.

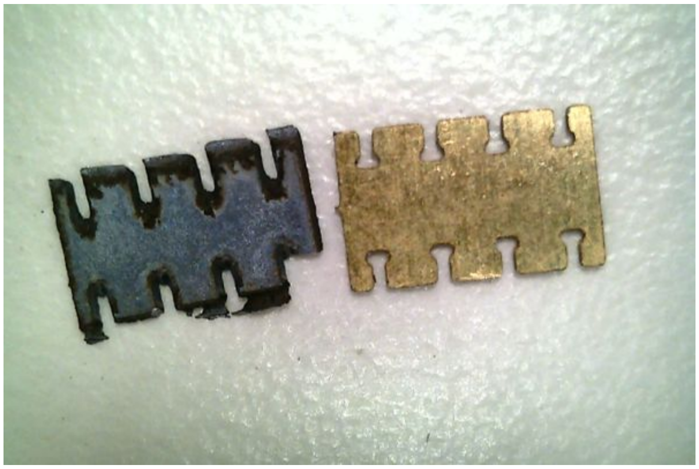

Figure 2-12: Excimer cut part next to brass part produced using the Wire-EDM.

Diamond Dicing Saw

Another approach I tried was to use a diamond dicing saw. This required splitting the part fabrication into two stages: first cutting out the rectangular part outline from a wafer, and then cutting slots in the sides for the press-fit joints. The silicon was fixtured in a Hurco VM10U 5-axis CNC and oriented such that the ⟨001⟩ flat was 45 degrees off center. This orientation ensures that the press-fit joints are oriented in the direction of most compliance, in order to reduce the likelihood of brittle fracture. [17] Rectangles with dimensions 0.25" x 0.488" were then cut from a 500 µm thick wafer. Figure 2-14 reveals that while there was some cracking in the ⟨001⟩ orientation, 25 parts were successfully cut out of a 4" wafer. The parts were then cleaned briefly in isopropyl alcohol to remove any residue from the fixturing tape.

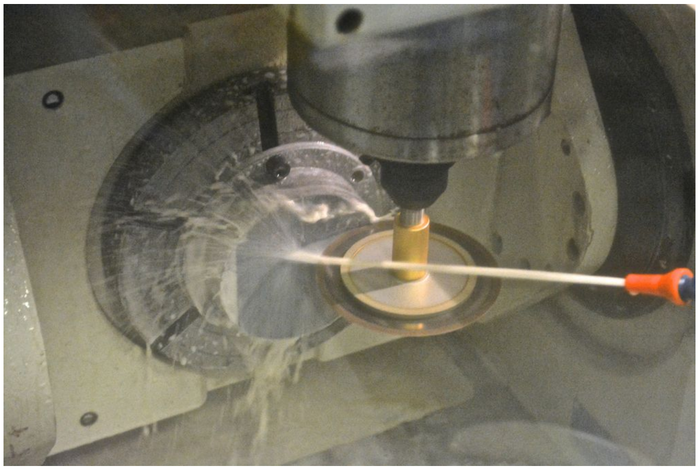

Figure 2-13: Dicing a silicon wafer in the Hurco VM10U.

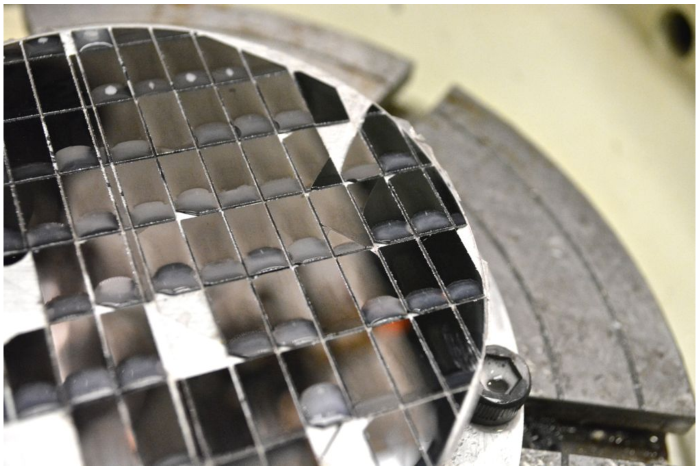

Figure 2-14: Close up of result of silicon wafer after dicing. Cracking is in the ⟨001⟩ > direction.

Looking at the parts under a microscope reveals that there is some chipping due to the dicing process. By climb-milling, chips are forced downward and out of the back of the cut so the bottom edge shows significantly more chip-out than the top surface, as is evident in figure 2-15.

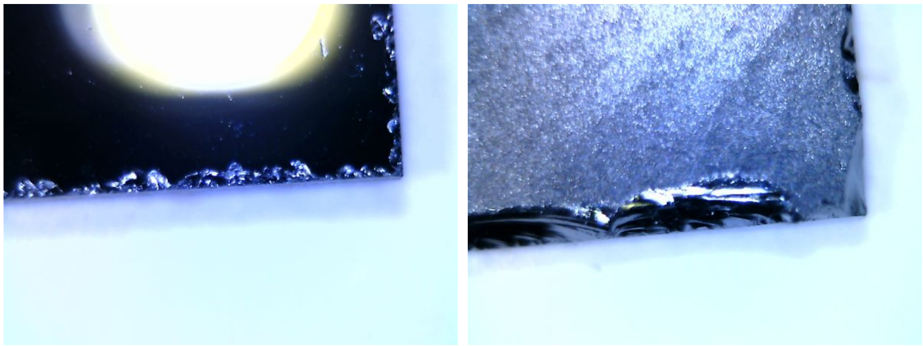

(a) Top surface edge

(b) Bottom surface edge

Figure 2-15: Showing close up of edge created by dicing saw. Some chipping is evident.

Once rectangles are cut from the wafer, they are refixtured in the machine to cut the press-fit slots. During this step, every single part experienced brittle fracture after the first slot was cut. I believe this is due in large part to the stress concentration that is created at the internal corner of the slot.

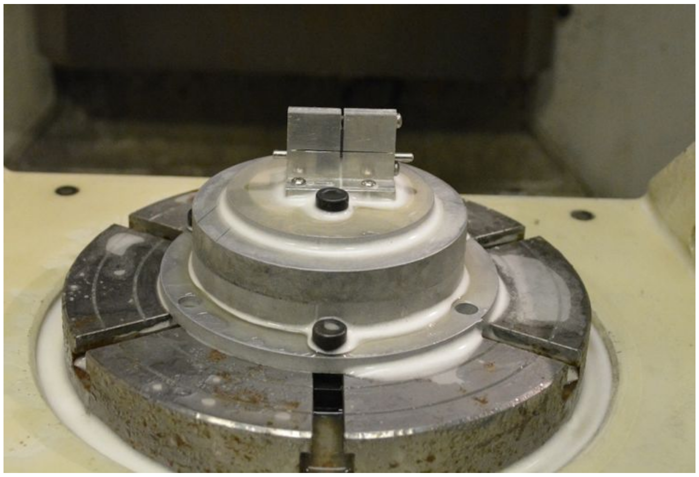

Figure 2-16: Fixture used to cut slots in the parts

Diode-Pumped Solid State Laser Machining

While the Excimer laser struggled to cut through the full thickness of a 500 µm silicon wafer, a diode-pumped solid-state (DPSS) 532nm laser is very well suited for bulk machining silicon. The higher wavelength and significantly faster repetition rates (50 kHz instead of 200 Hz) allow parts to be cut much faster and with many fewer problems such as debris build up, recast material, and heat affected zone.

Figure 2-17 shows two SEM micrographs of a slot cut using a 6 W DPSS laser. It is clear that the laser produces an incredibly smooth and precise cut.

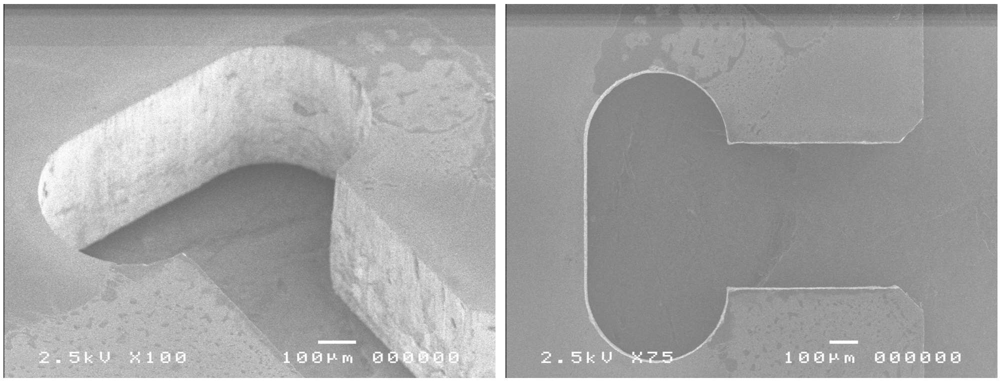

(a) Figure A

(b) Figure B

Figure 2-17: A SEM micrograph of the slot of a part made with the DPSS laser from Oxford Lasers, Inc. [1]

Micro-Waterjet

Waterjet abrasive machining uses a high pressure jet of water mixed with abrasive to cut through many different types of materials—from wood, plastics, and metals to brittle materials such as acrylic, glass, and stone. The OMAX MicroMAX JetMachining Center has a kerf width of approximately 0.020 in, which is an appropriate size to produce parts from standard 500 µm silicon wafers. [25]

Figure 2-18 shows a comparison between a slot made with the micro-waterjet and one made with the DPSS laser. The slot made with the waterjet shows some edge rounding on the top face and chip-out on the back face.

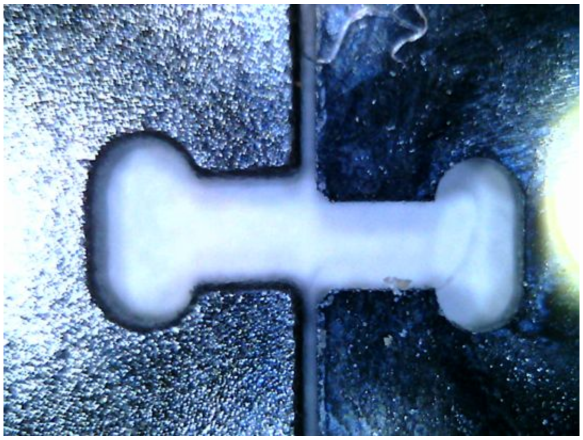

Figure 2-18: A slot made with the microwaterjet (left) compared with one from the dpss laser (right)

Deep Reactive Ion Etching

Deep reactive ion etching (DRIE) is a cleanroom process that uses a sequence of etches and polymer depositions to produce very high aspect ratio (> 30) features from materials like silicon. That is to say, a 15 µm channel could be etched through a 500 µm thick silicon substrate. Figure 2-19, for example, shows high aspect-ratio gears fabricated using the Bosch process.

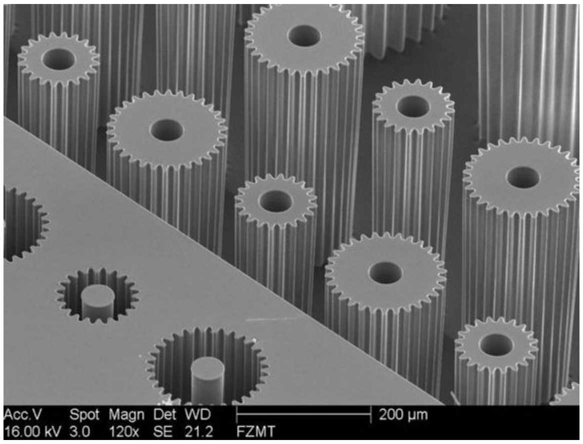

Figure 2-19: High aspect-ratio gears made with DRIE. [33]

This process is very well suited to batch produce many press-fit silicon parts at once with very precise tolerances.

Chapter 3

Discretely Assembled Circuits

The first step in demonstrating the ability to assemble structures with electronic functionality is to be able to electrically connect various parts of the structure, or, in other words, to assemble circuits.

3.1 Three-Dimensional Electrical Networks

Using just two part types (insulating and conducting) it is possible to fabricate arbitrary electrical networks through three-dimensional structures.

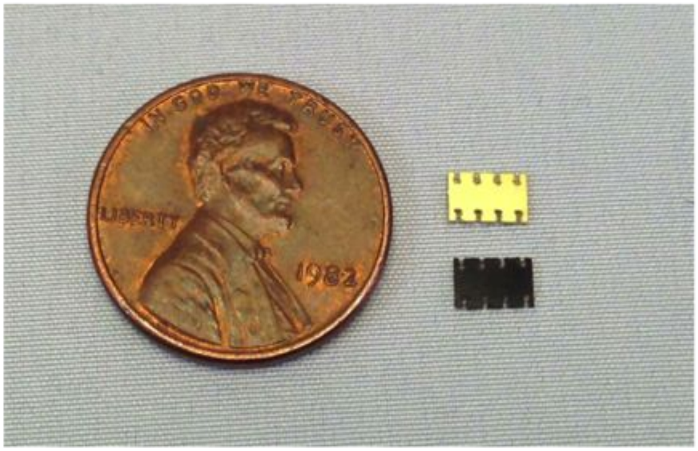

Figure 3-1: The two part types needed to make an arbitrary 3D circuit.

To demonstrate this idea I built a “hello world” example that uses a small microcontroller to flash an LED on and off. The entire circuit is fabricated from reversibly assembled press-fit parts.

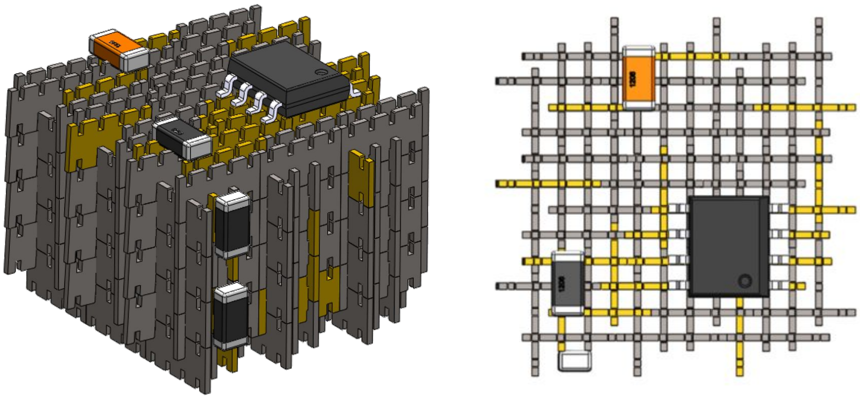

(a) Isometric view

(b) Top view

Figure 3-2: Discretely assembled circuit render.

3.1.1 Design

Discretely assembled circuits cannot be designed in the same way that conventional printed circuit boards are designed, since the structures are inherently three-dimensional and are constrained by a lattice. Furthermore, in addition to creating the required conductive pathways, the assembly needs to be designed in such a way that it is structural. This structural integrity comes in large part from the staggering of parts in subsequent rows and columns such that the seams between parts do not cut across the entire assembly.

In order to design this “hello world” circuit, I used an image editing program to layout a grid representative of the assembly lattice. I then added the components that were to be connected as a layer on top of the grid. Working from the top down it was possible to sketch, layer by layer, where the conductive parts needed to be placed with respect to the insulating ones, in order to make the desired electrical connections. The top few layers of the circuit design are shown in Figure 3-3 where the lighter colored blocks represent conductive parts and the darker ones represent insulating ones. The different colors represent different layers of the object.

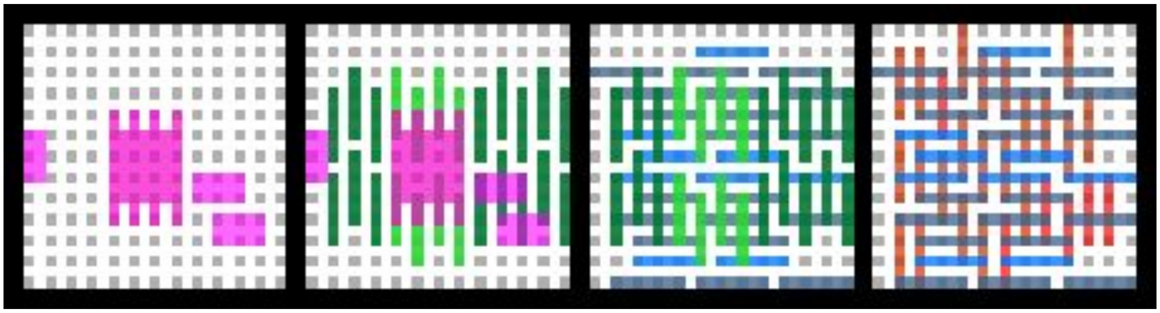

Figure 3-3: The top few layers of the design of a discretely assembled circuit.

3.1.2 Assembly

The circuit was assembled by hand with tweezers. Once the first two-layers were built the structure was relatively sturdy and assembly could proceed much more quickly.

The Atmel ATtiny45 microcontroller was pre-programmed to toggle an output pin on and off before being soldered onto the assembly. All components necessary for the circuit's function reside in the assembly apart from two AA batteries which supply the power to the circuit.

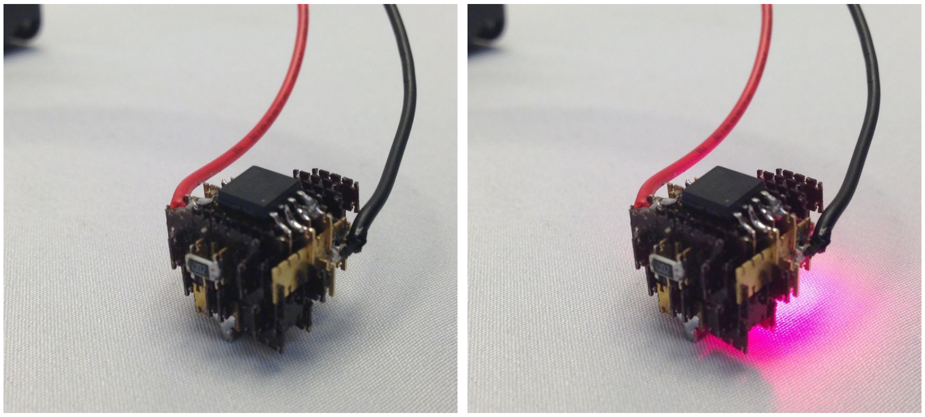

(a) LED off

(b) LED on

Figure 3-4: Discretely assembled circuit board blinks an LED on and off.

Chapter 4

Discretely Assembled Passive Components

Given the ability to make arbitrary three-dimensional circuitry, the next step in demonstrating digital assembly as a means of fabricating microelectronics is to show the construction of passive components.

Passive components are electronic components that cannot introduce energy into a circuit; they are not capable of power gain. Perhaps the three most important passive components are the capacitor, inductor, and resistor.

In this section I look at how these three components may be discretely assembled from three types of parts: a conductive part, an insulating part, and a resistive part. The geometry by which the part-types are arranged in the structure determine its electrical behavior. The capacitor, for example, may be assembled by placing the conductive parts in an interdigitated finger arrangement while the inductor is assembled by placing the conductive parts in a loop or helix arrangement. Resistors are simply assembled by placing resistive material in either a series or parallel arrangement in order to achieve the desired resistance.

4.1 Analysis

4.1.1 Capacitors

The capacitance of an assembled structure can be roughly approximated by summing the capacitances of a series of parallel plates. The capacitance of a single parallel plate capacitor can be expressed by the equation:

$$C = \frac{\epsilon A}{d} \tag{4.1}$$

where A is the area of the plates, d is their spacing, and ϵ is the dielectric permittivity of the medium between the plates.

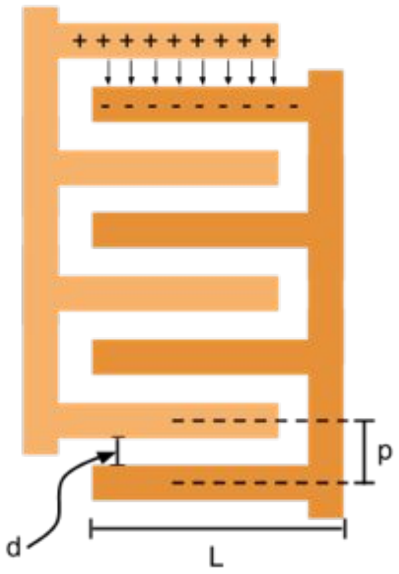

Figure 4-1: A diagram of a discretely assembled interdigitated capacitor (top-down view).

Let us consider a small assembly of conductive parts arranged in an interdigitated finger arrangement like that of Figure 4-1. For a unit such as this, we can approximate its capacitance and see how it scales by plugging in part dimensions into the basic formula for a parallel plate capacitor.

$$C = n\frac{\epsilon(l \times h)}{d} \tag{4.2}$$

Where n is the number of parallel plate fields in the geometry, l is the length of the part, h is the height of the part, and d is their spacing. We can substitute the length, height, and gap spacing by multiples of a characteristic length, the pitch of the lattice: p. In the case of the standard part shape I have dealt with in this work: $l = 4p$, $h = 2.5p$, and $d \approx p$.

$$C = n\frac{\epsilon(4p \times 2.5p)}{p} \tag{4.3}$$

This then simplifies to

$$C = 10\epsilon np \tag{4.4}$$

which shows that capacitance scales linearly with the characteristic length of the lattice (p in Figure 4-1). However, because volume decreases with the cube of the characteristic length, there are large wins in efficiency (capacitance per cubic volume) when scaling down.

4.1.2 Inductors

Inductance can be created by the placement of conductive parts in loops.

The inductance of an air filled coil can be roughly approximated by the following equation:

$$L = \frac{d^2n^2}{18d + 40l} \tag{4.5}$$

where L is inductance in μH, d is coil diameter in inches, and l is coil length in inches. [19] Using this, we can calculate the inductance of one loop of a discretely assembled inductor:

$$L = \frac{d^2}{18d + 40l} \tag{4.6}$$

We can then define the variables of this equation in terms of measurements of a discrete part. So, $d \approx 4P$ and $l \approx 5P$.

$$L = \frac{(4p)^2}{18(4p) + 40(5p)} \tag{4.7}$$

This then becomes

$$L = 0.05882p \tag{4.8}$$

Finally, by setting $P = 1.27\,\text{mm}$ we find that $L = 2.94 \approx 3\,\text{nH}$ per loop.

4.1.3 LC Resonators

By combining these three components, an LC resonator can be assembled. The resonator can be made by either a series or parallel combination of the capacitor and inductor and can be designed to resonate at a particular frequency. Depending on how it is designed, this resonance can also be used to create a number of different types of filters including low-pass, band-pass, high-pass, and notch.

An important measurement of LC resonators is their quality factor. The quality factor gives an indication of how selective (sharp) the resonance is. High-Q resonant filters are often desirable because they have better selectivity and lower insertion loss. [6]

The Q of a resonator can be calculated from the values of the sub-components that comprise it. For a series RLC circuit this is

$$Q = \frac{\omega_0 L}{R}$$

where ω_0 is the resonant frequency which occurs at $1/\sqrt{LC}$ for any kind of LC resonator.

It is clear then that the Q is in large part determined by the inductor and its series resistance.

4.2 Assembly

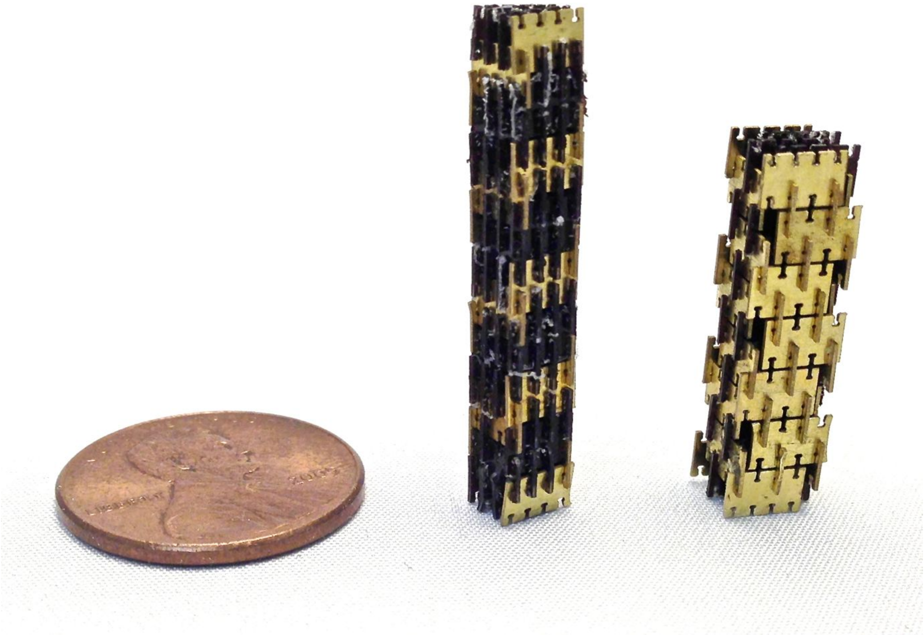

Figure 4-2: A discretely assembled inductor (middle) and capacitor (right) next to a penny for scale.

I assembled the discrete passive components in much the same way as the circuits, using hand tools such as micro-pliers and tweezers. Given the scale of the parts and the previous analysis, tens of picofarads and hundreds of nanohenries are achievable by assembling these structures by hand. Figure 4-3 shows a capacitor being assembled on a brass substrate.

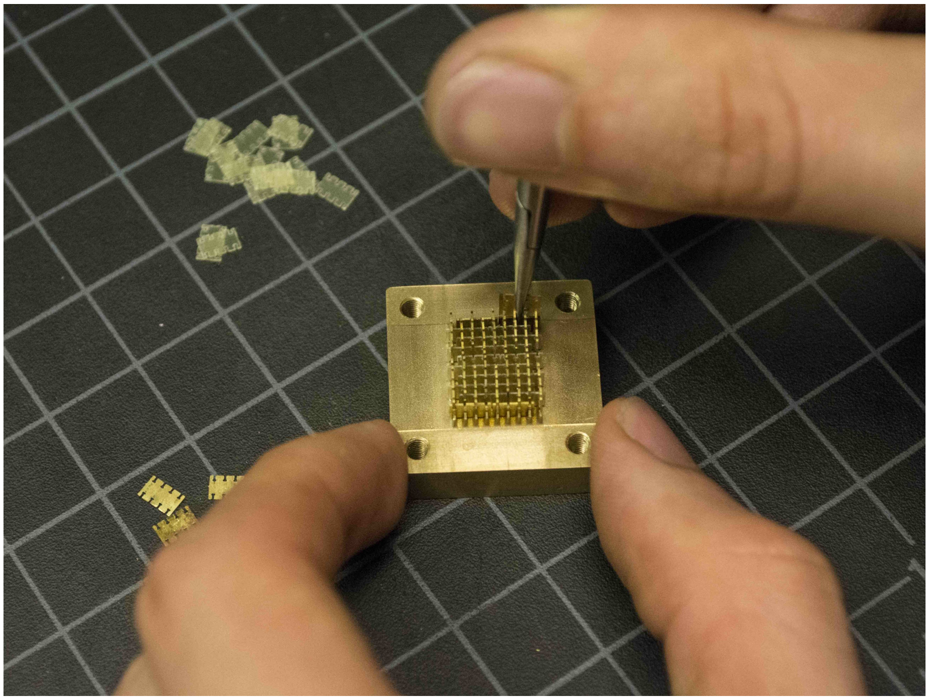

Figure 4-3: Assembling a discrete capacitor

Initial prototypes (like those shown in Figure 4-2) were built freestanding. As the assemblies grew larger and I found that the joints needed preloading, I introduced a substrate. The brass substrate is made on the wire EDM and serves as a base on which to build the structure, an electrical connection to the parts of the discretely assembled component, and a pre-loading package to increase the conductance of the joints. For those components for which a conductive substrate would interfere significantly with the electronic functionality, an epoxy substrate was used. This substrate was made by creating a PDMS mold from the brass positive and then casting an epoxy resin to create the electrically insulating substrate.

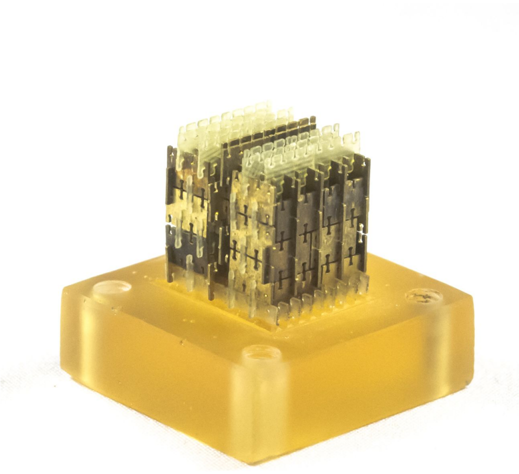

Figure 4-4: An epoxy substrate serves as an electrically insulating substrate.

The value of the discretely assembled capacitors is determined by the number of conductive parts (and therefore the number of parallel plate fields) that make up the assembly. For example, Figure 4-5 shows a series of capacitors that range in value from a few picofarads to 20 pF.

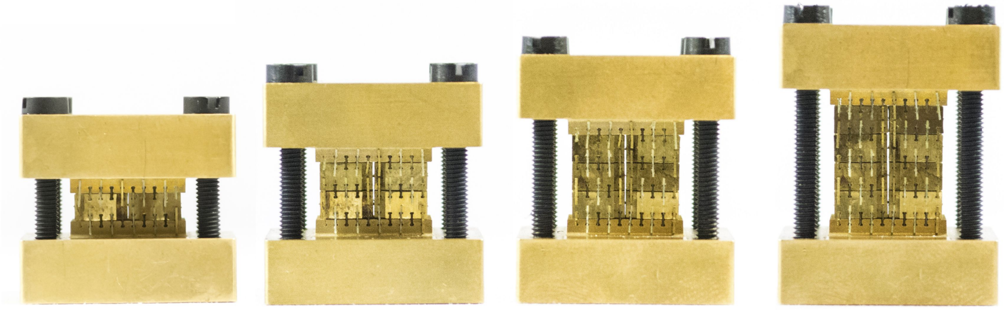

Figure 4-5: A family of discretely assembled capacitors

The inductor is composed of an array of seven coils, each coil having two to three turns. Figure 4-6 shows a discretely assembled inductor along with an X-ray view of its interior.

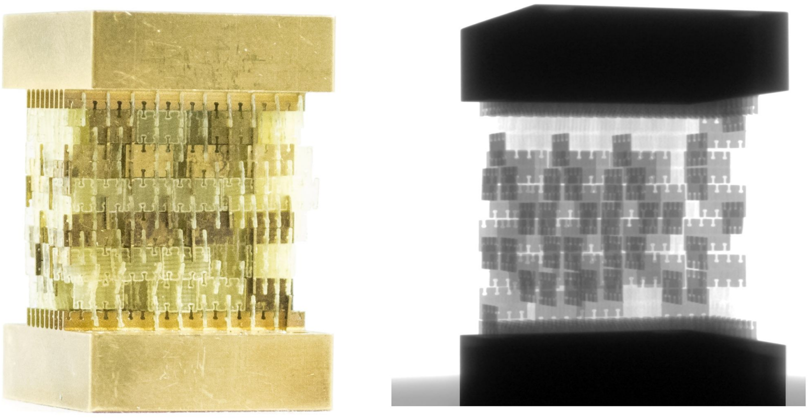

Figure 4-6: A discretely assembled inductor with an x-ray view of the interior.

A discretely assembled resistor made from anti-static polymer parts is pictured in Figure 4-7. The resistive parts are all connected in parallel bringing the resistance down from 100 kΩ of a single part to approximately 5 kΩ.

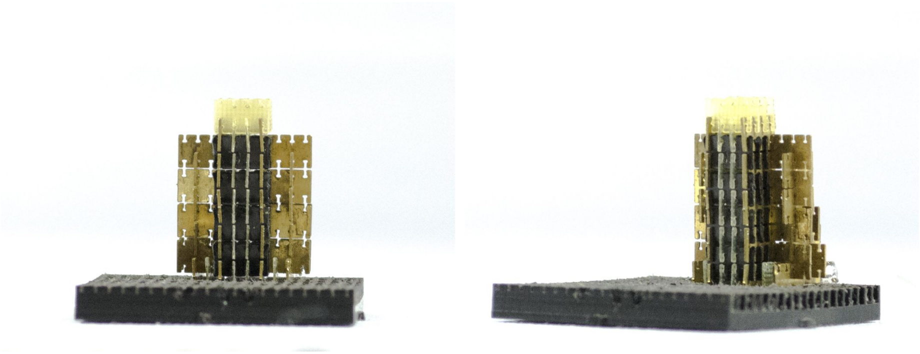

(a) Front view

(b) Angled view

Figure 4-7: A discrete resistor asssembled from anti-static polymer parts.

4.3 Evaluation

4.3.1 LCR Meter

In order to determine the approximate value and quality of the assembled component, I used an LCR meter to measure the complex impedance of the structures. The angle of the complex impedance gives an indication of how pure (and free of parasitics) the component is.

$$Z = |Z|e^{j\phi} \tag{4.9}$$

$$\phi = \arctan\frac{X}{R} \tag{4.10}$$

The largest capacitor shown in Figure 4-5 has an impedance of $Z_c = 8.13 \times 10^4 e^{j(-89.53^\circ)}$. An ideal capacitor would have an impedance angle of -90° such that it is purely reactive and has no series resistance. This impedance can be transformed into a measure of capacitance given that there is a known test frequency. In this case, the capacitor measured 19.6 pF.

Looking at a series of capacitors, we can confirm that the capacitance of the assembly scales linearly with the number of conductive parts that comprise it. Figure 4-8 shows that roughly 1.3 pF is added for every six conductive parts.

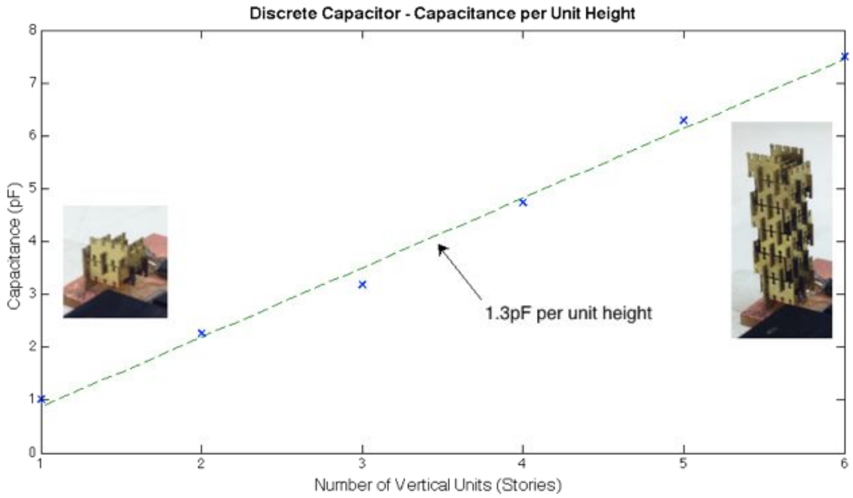

Figure 4-8: A plot showing how capacitance scales linearly with the number of conductive parts assembled.

The inductor pictured in Figure 4-6 was measured to have an impedance of $Z_L = 4.83 \times 10^{-1} e^{j(35.1^\circ)}$. An ideal inductor has an impedance angle of 90°. This, however, is impossible to achieve in practice. Instead, component designers strive to produce inductors with a high quality-factor (or Q). The Q of an inductor relates the reactance and resistance of the component at a particular frequency.

$$Q_L = \frac{\omega_0 L}{R_L} \tag{4.11}$$

In this case, at 100 kHz the inductor exhibits a Q-factor of roughly 0.7. This compares favorably to a standard surface mount inductors which was measured to have a quality factor of 0.5 at this frequency but was slightly less than a precision inductor, which achieved a Q of 0.8.

4.3.2 Frequency Response Analysis

To evaluate the performance of the discretely assembled passive components at various frequencies, I conducted a frequency response analysis and measured the attenuation and phase shift of a sinusoidal input source over a number of frequencies ranging from 10 kHz to 150 MHz.

An Agilent E4421B ESG series signal generator was used to generate the input signal. A Tektronix MS02024 oscilloscope was used to measure both the input and output signal. Four measurements were recorded at each frequency: the frequency, the amplitude of the input, the amplitude of the output, and the phase shift between the input and output.

Capacitor

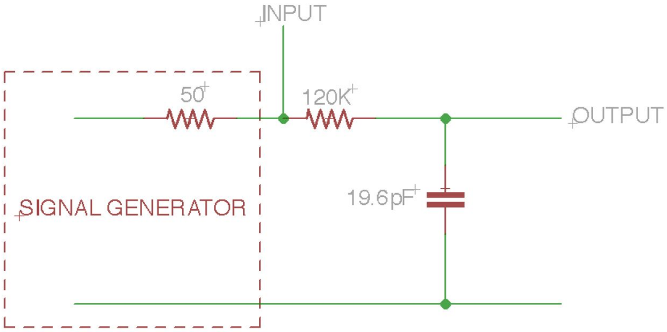

Figure 4-9: The RC circuit used to measure the frequency response of the capacitor.

In this configuration the circuit acts as a low pass filter where the corner frequency is $\omega_c = 1/RC$. At low frequencies the output signal matches the input signal but as the frequency is increased past the corner frequency, the output signal is attenuated and phase shifted. Figure 4-10 shows the frequency response of the discretely assembled capacitor. The dash-dot line shows the simulated results based off of the pre-measured component values; these were measured with the LCR meter at 100 kHz.

It is clear that the experimental results are in-line with the simulation. At very high frequencies there are deviations from the expected results due to the fact that the highly-attenuated output signal becomes difficult to measure.

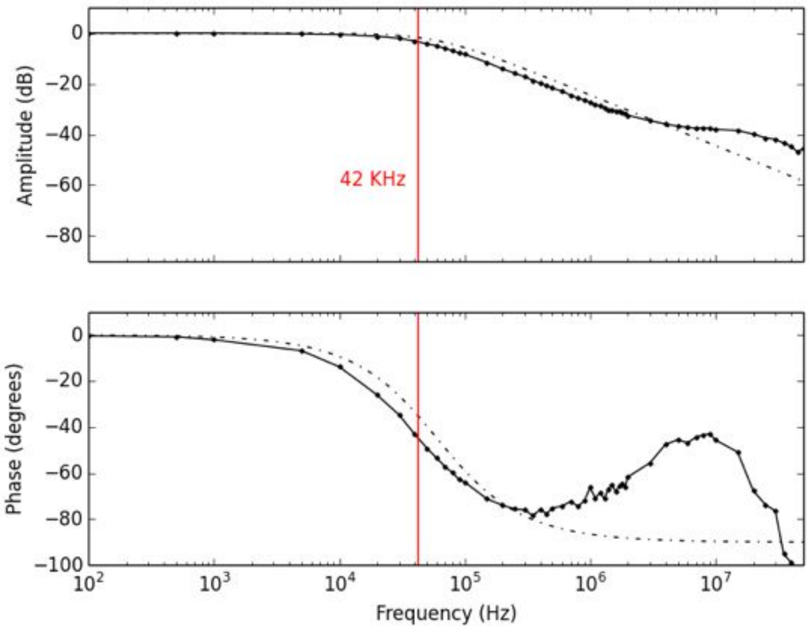

Figure 4-10: A bode plot showing amplitude and phase shift of a capacitor.

Inductor

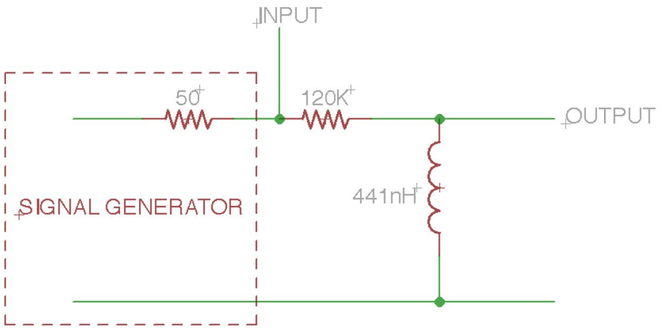

Figure 4-11: The RL circuit used to measure the frequency response of the inductor.

In this configuration the circuit acts as a high pass filter where the corner frequency is $\omega_c = R/L$. Figure 4-12 shows the frequency response data collected for the discretely assembled inductor. Again, it closely matches the simulated result but diverges where the amplitude of the output signal is too low to properly measure.

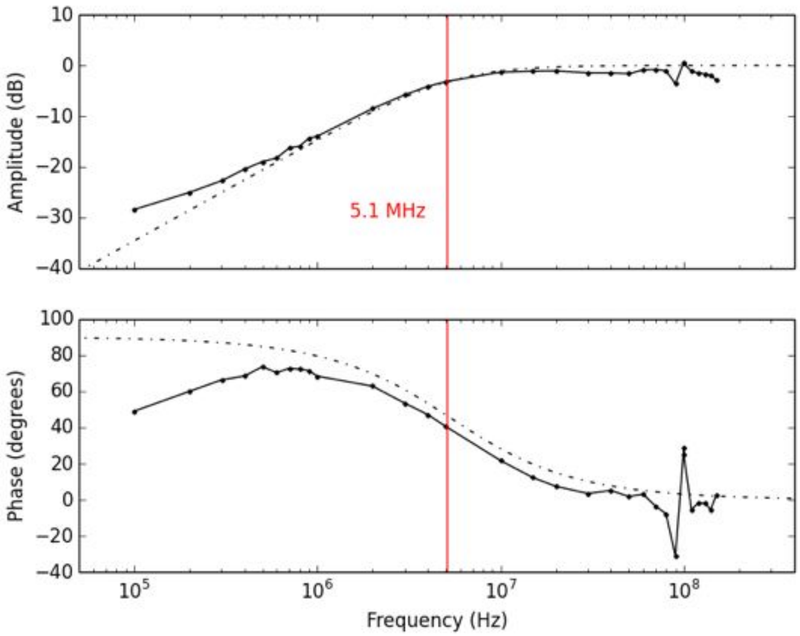

Figure 4-12: A bode plot showing amplitude and phase shift of a inductor.

LC Resonator

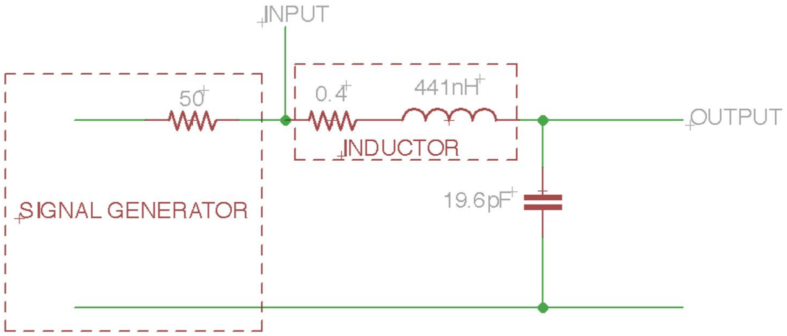

INPUT
50
0.4
441nH
OUTPUT
INDUCTOR
19.6pF
SIGNAL GENERATOR

Figure 4-13: The RLC circuit used to measure the frequency response of the LC Resonator.

In this configuration the LC circuit acts as 2nd order low pass filter. At low frequencies the output matches the input but after a resonant peak at $\omega_r = 1/\sqrt{LC}$ the signal becomes sharply attenuated.

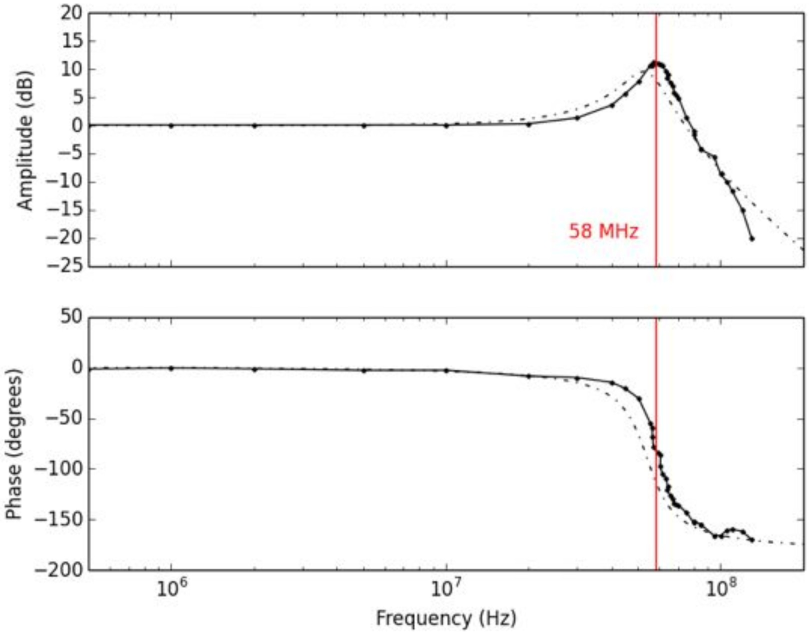

Figure 4-14: A bode plot showing amplitude and phase shift of an LC resonator.

Zooming in on the resonant peak, it is possible to calculate a quality factor which is not frequency dependent. The quality factor of the resonator can be found with the following equation.

$$Q = \frac{f_r}{\Delta f} \tag{4.12}$$

where f_r is the resonant frequency and Δf is the half-power bandwidth of the resonant peak. This is the frequency bandwidth over which the power of the peak is reduced by half (or 3dB). Figure 4-15 shows a close up of the resonant peak where the relevant parameters can be extracted to determine the Q of the resonator.

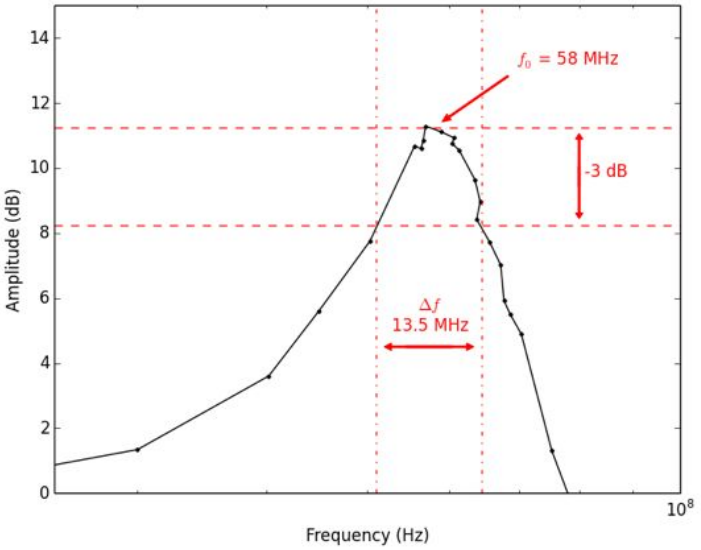

Figure 4-15: Q-Factor analysis of the LC Resonator.

In this case, the circuit was found to have a quality factor of 4.3. While this seems low, the measured Q has been loaded with a 50 Ω source impedance from the signal generator. This greatly lowers the Q of the resonator. By simulating the resonator without the source impedance, I found that the Q should be upwards of 109.

In comparison, I measured an LC resonator constructed with commercially available components of similar values (a 0.44 µH inductor and a 19.6 pF capacitor) and found its 50 Ω loaded Q-factor to be approximately 10.5.

To achieve higher Q-factors, the quality of the discretely assembled inductor needs to be improved. Because, it is constructed from the series combination of conductive parts (placed in loops), it is very sensitive to defects at the interface between parts. Installing the inductors in packages to provide high amounts of preload is one way to mitigate this problem. Another alternative, would be to rethink the part-design for inductors. The vertically assembled parts used in this work are not optimized for creating spiral loops; one could envision other part-types that enable the construction of much denser, higher quality inductors.

Chapter 5

Discretely Assembled Active Components

Proving digital assembly as a viable microelectronic fabrication process means showing it can not only create circuitry and passive components, but also active components like diodes and transistors.

Unlike passive components, active components are nonlinear, and therefore, enable amplification. This amplification is what makes possible digital logic; whereby small signals can control large ones. This is, in essence, what a transistor does.

In this section I explore ways two active devices (a Schottky diode and a MOSFET) may be constructed from discrete semiconducting parts.

5.1 Analysis

5.1.1 Schottky Diode

A Schottky diode may be formed by creating a rectifying metal-semiconductor junction. This kind of junction is formed when a semiconducting part is connected to a metal part. Care needs to be be taken to ensure the right metals and doping levels are chosen such that one connection makes an ohmic contact (a constant low resistance) and the other forms the Schottky barrier. [2]

The current through a Schottky diode can be roughly approximated with the equation:

$$I = I_{sat}(e^{(qV/kT)} - 1) \tag{5.1}$$

where I_{sat} is the saturation current governed by:

$$I_{sat} = A \times KT^2 e^{(-q\phi_b/kT)} \tag{5.2}$$

where A is the diode area, K is the Richardson constant, q is charge, ϕ_b is the potential barrier, k is the Boltzmann constant, and T is the temperature. [9]

A Schottky diode's barrier height is tunable based on what metal is chosen to create the Schottky barrier. In this case, I have chosen to use copper which has a potential barrier height of 0.35eV with respect to n-type silicon. For the ohmic contact, I have chosen to use aluminum which has a potential barrier height of 0.2eV with n-type silicon.

The above equations, however, do not take into account non-ideal characteristics such as parasitic resistance due to contact resistance. To include these real-world characteristics requires a nonlinear equation where the solution is found iteratively. For example, the diode equation can be updated to include the series resistance, R_s and an ideality factor, n.

$$I = I_{sat}(e^{(q(V-IR_s)/nKT)} - 1) \tag{5.3}$$

I used the SPICE diode model to simulate less-ideal diode constructions. Here, a diode can be specified with a series resistance, an ideality factor, and a number of other characteristics like a parasitic capacitance.

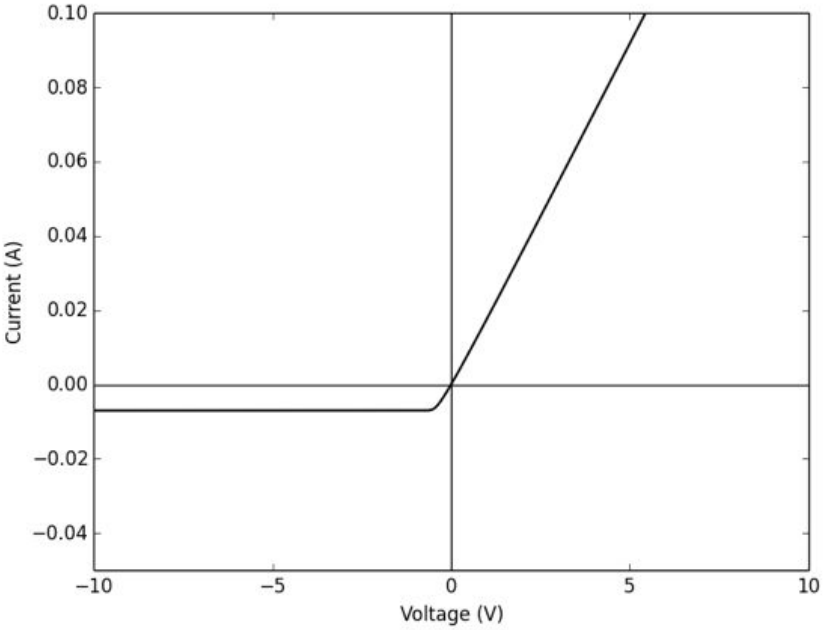

Figure 5-1: A simulation of a diode made with copper and aluminum.

In this case the diode simulation assumes a series resistance of $50\,\Omega$, a diode area of $6.45 \times 10^{-4}\,\mathrm{cm}^2$, and an ideality factor of 2.

5.1.2 MOSFET

A transistor is the critical building block in making a microprocessor. There are a number of different types of transistors but I have focused specifically on what is required to assemble a metal-oxide-semiconductor field-effect transistor, or MOSFET. This kind of transistor is able to switch large currents with small voltages and is used in a vast majority of modern digital circuitry.

In an enhancement mode MOSFET, a voltage at the gate electrode controls a conducting channel between the source and drain contacts. The distance between the gate electrode and the channel is a critical parameter. In conventionally produced MOSFETs this distance can be as small as one nanometer.[8] In a discretely assembled diode we can use the lattice spacing to set this distance.

All four types of semiconducting part-types are needed to create a functional

MOSFET. For an N-MOSFET, P-type silicon serves as the substrate. Two N-type parts make contact with the substrate and serve as the source and drain. In order to ensure ohmic contacts, N+ silicon parts may be used to interface between the N-silicon and the rest of the circuit. Similarly, a P+ silicon part may be used to connect the source and the substrate to eliminate body bias.[8] The render shown in Figure 5-2 shows an N-MOSFET which is made with a P-type substrate.

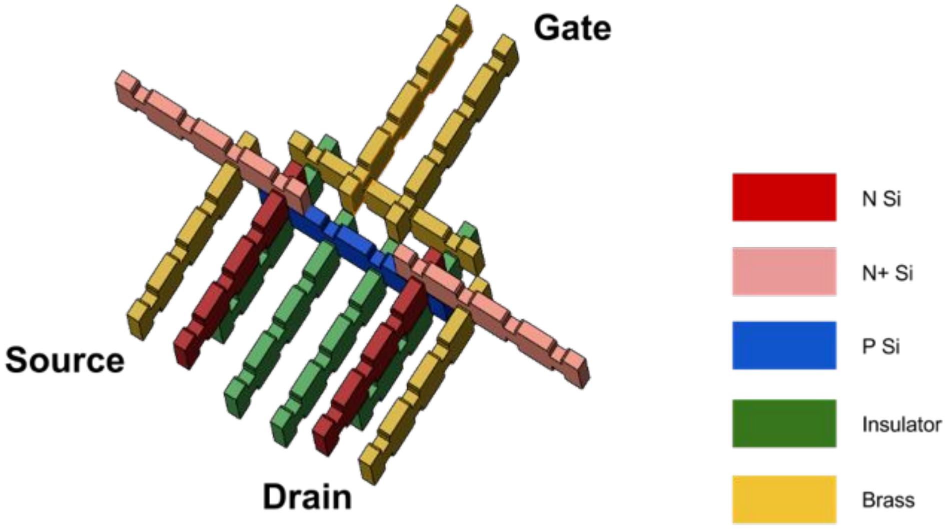

Figure 5-2: A schematic render of how a MOSFET could be discretely assembled.

5.2 Assembly

Because silicon is so brittle, assembly of semiconducting devices is unlike the assembly circuits and passive components. Success depends crucially on the tolerance of the press-fit slots and the minimization of off-axis forces during assembly. Figure 5-3 shows a successful and failed Schottky diode assembly attempt. In this case, the problem of assembly is exacerbated when the silicon part needs to join with more than one other part.

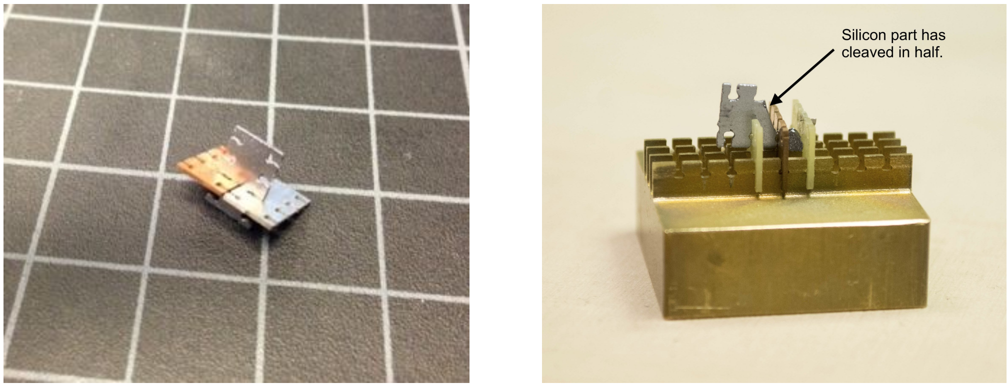
Silicon part has cleaved in half.

Figure 5-3: Two Schottky diode assemblies: a successful press-fit connection (left), a failed press-fit part insertion (right).

In order to improve the assembly of silicon parts, a number of different techniques may be employed. For example, flexures can be designed into the part to allow more compliance between parts. Precedent for flexural snap-fitting silicon exists at the MEMS scale and should scale to this size. Alternatively, one could use high-temperatures to thermally relax the silicon and put it in a more ductile state. This has the drawback of possibly spurring growth of an oxide layer that would inhibit electrical connections.

Because of the difficulty of assembly, I decided work around the press-fit assembly and conduct an experiment with a planar diode construction to determine how well a diode made with purely mechanical connections (without annealing) can function. The diode is simply made by sandwiching N-type silicon between aluminum and copper and applying a large clamping force to increase effective contact area.

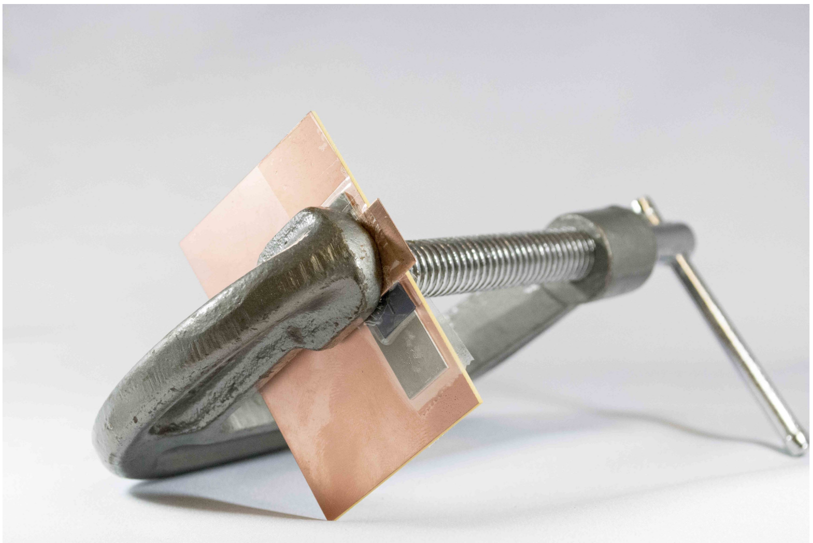

Figure 5-4: The clamped diode's construction.

5.3 Evaluation

Evaluation of the clamped Schottky diode was performed with an HP4155A semiconductor parameter analyzer. The voltage was swept from -10V to 10V and the current through the device under test was measured. Figure 5-5 shows the diode's IV characteristics.

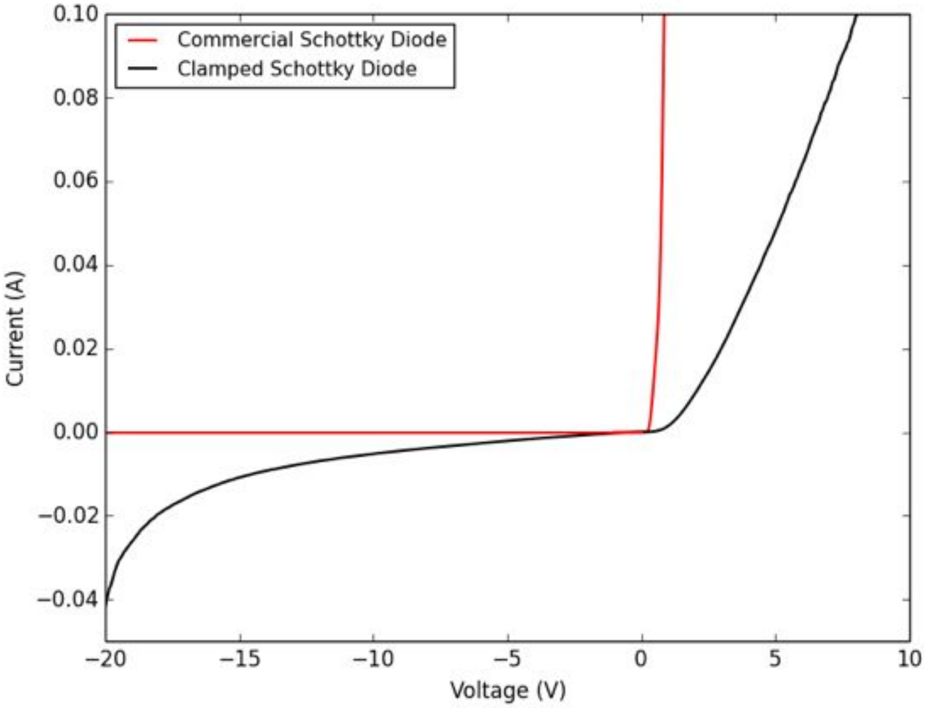

Figure 5-5: The clamped diode's IV characteristics.

It is clear that the device exhibits diode behavior. The turn-on voltage occurs at roughly 2 V where the current begins increasing exponentially before linearizing because of series resistance. Reverse breakdown is also evident as voltages below −15 V begin to allow more current through.

Chapter 6

Simulation

For digital assembly of electronic structures to be scalable to larger structures made of smaller parts, there needs to be some way of simulating a structure's electrical performance before constructing it.

Given how different the digital assembly technique is from current state-of-the-art microelectronic fabrication processes, the design and simulation tools will be similarly different and new methods of designing and characterizing these structures will need to be developed.

At the scale of structures that are able to be assembled by hand, current design and simulation tools can be used. This section details two simulation approaches that I used throughout the course of this work.

6.1 COMSOL Modeling

At low frequencies, we can use a multiphysics environment like COMSOL to get a reasonable estimate of a structure's performance before it is built.

Starting with simple primitives like parallel plate capacitors and a single inductor loop, we can move on to model larger assemblies like the the inductor coils pictured in Figure 6-2.

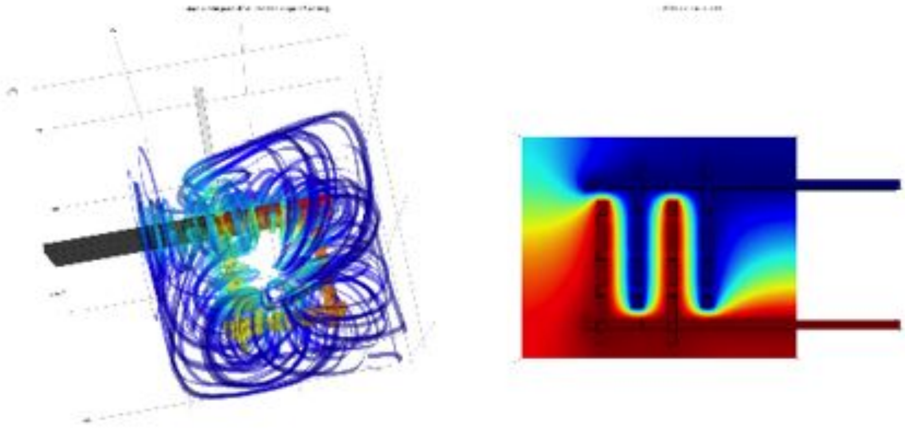

Figure 6-1: Modeling a single inductor loop and interdigitated parallel plates

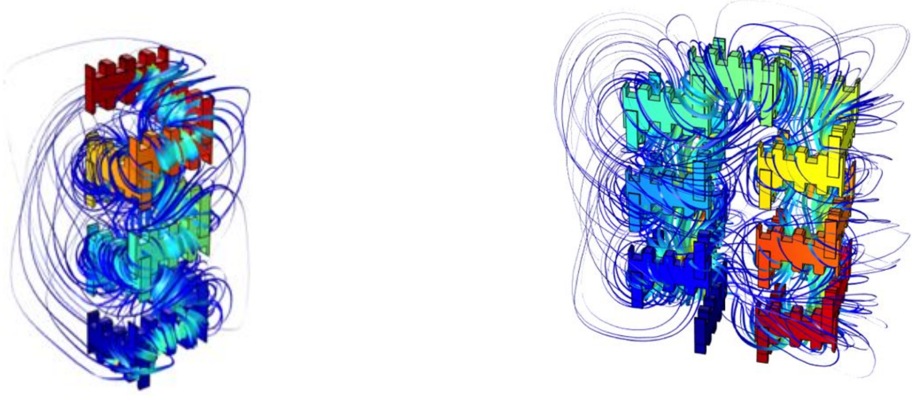

(a) Single spiral inductor

(b) Two spiral inductor

Figure 6-2: COMSOL modeling of small inductor assemblies. The single spiral inductor (left) has an inductance of 5.1 nH while the two spiral inductor (right) has an indutance of 13.9 nH

Whole assemblies of complex impedance circuitry can also be simulated. Figure 6-3 simulates an LC resonator assembly. By determining the approximate values of the components, the electrical behavior of the real assembly can be predicted.

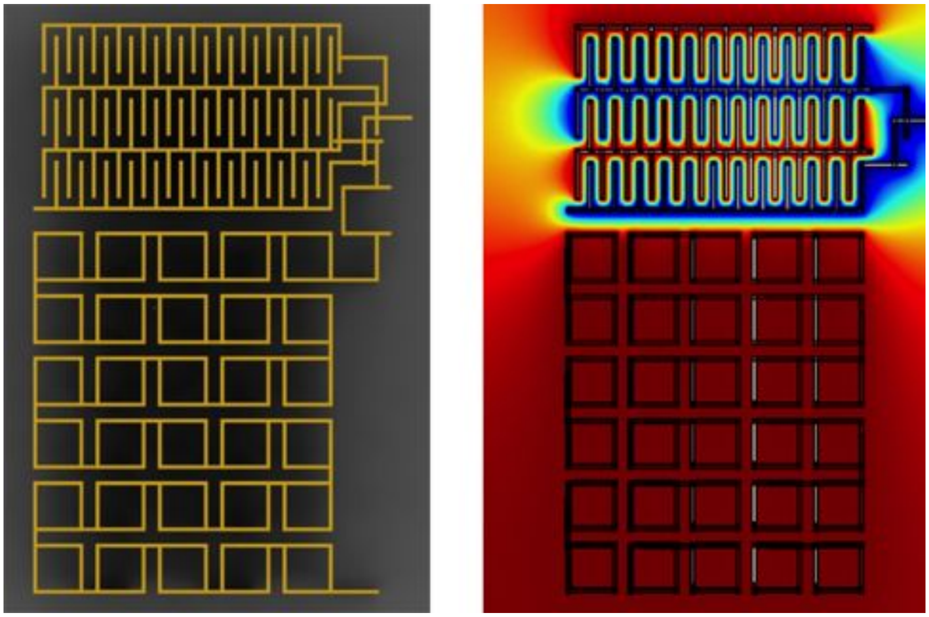

Figure 6-3: Electromagnetic modeling of LC resonator.

Multiphysics modeling such as this also presents a good method of checking where electrical parasitics come from. For example, in modeling the LC resonator, I determined that by shifting the inductive part of the assembly away from the capacitive part of the assembly by one pitch, I reduced the parasitic capacitance developed at the interface significantly.

6.2 FDTD Solver

To determine how the structures behave at high frequencies, we can use a finite-difference time-domain (FDTD) solver to solve Maxwell's equations in three-dimensions. This is useful, for example, in designing antennas, RF circuits, and metamaterials.

I implemented the FDTD solver in C and wrote a Python wrapper to compile and execute the C-code, import the data, and render the results using Mayavi. To validate the calibration of the solver I simulated a plane wave hitting a dielectric sphere. This is a problem that can be solved for analytically using Bessel function expansions. [30] Figure 6-4 shows the results of this simulation. I found that the Bessel function expansion closely matched the simulation results.

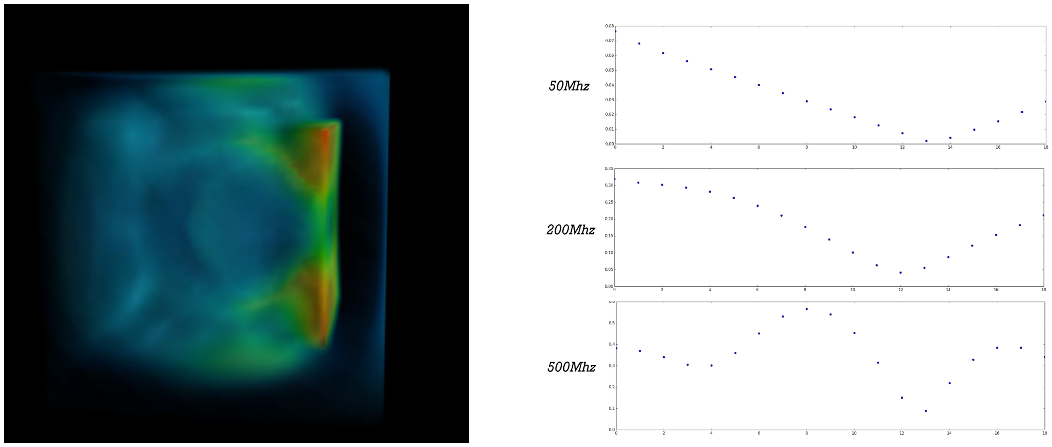

(a) Plane wave hitting a dielectric sphere

(b) Field Strength vs horizontal position

Figure 6-4: FDTD solver validation

Geometry can be input into the solver from a GIF image file in which the dielectric constant of a voxel of material is represented by the grayscale color value of the respective pixel. Figure 6-5 and Figure 6-6 show simulations of two different planar antenna geometries.

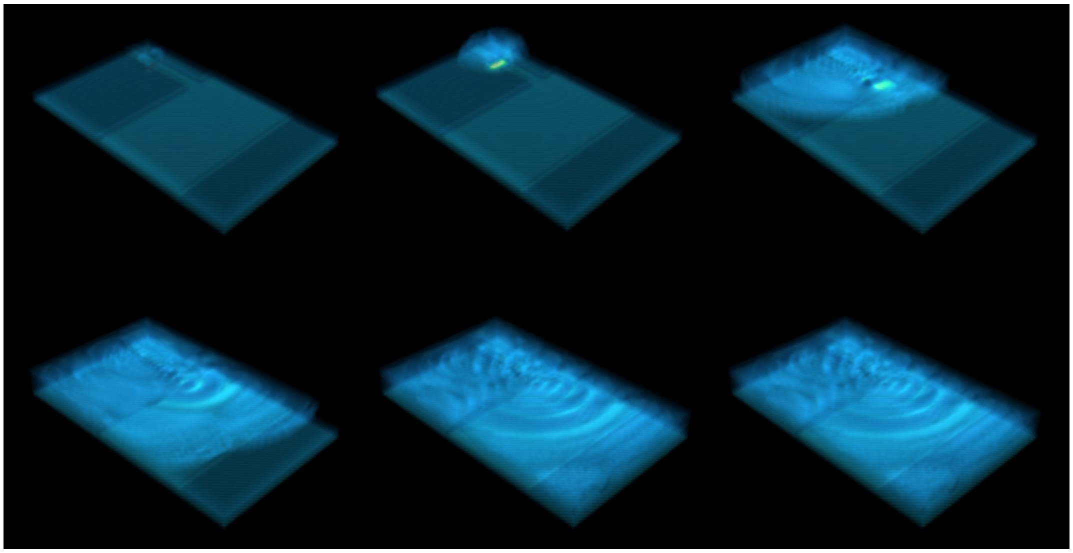

Figure 6-5: FDTD simulation of a micro-patch antenna.

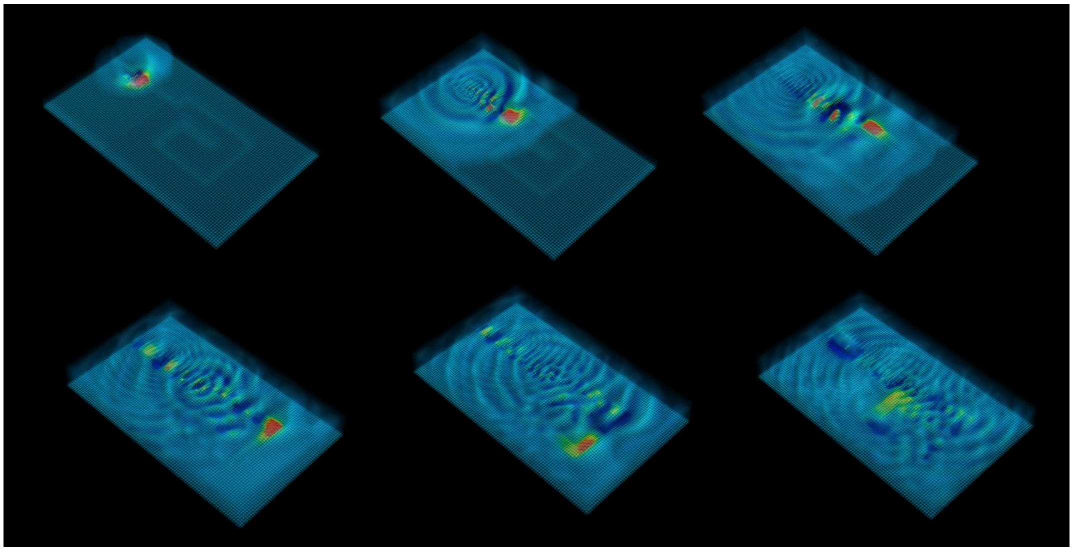

Figure 6-6: FDTD simulation of a spiral chip antenna.

The value and quality of the antenna can be determined by looking at the Fourier transform of the reflected wave, the S_{11} parameter. The antenna is well designed for a particular frequency when the amplitude of the reflectance is sharply attenuated at that frequency (the signal is maximally radiated into space).

Chapter 7

Evaluation and Measurement

In order to show that electronic digital materials are viable as a means of producing microelectronics, the mechanics at the interface between parts needs to be understood, and needs to ensure reliable and repeatable electrical contacts.

The quality of the electrical contacts is crucial not only for reliable circuitry, but also for reducing parasitics and improving the quality factor of the assembled components. This section details the measurement and evaluation of the electrical interfaces between parts.

7.1 Contact Resistance

Minimizing the contact resistance of the joints in a structure like this is crucial in achieving scalable electronic performance.

At low frequencies, the constriction resistance at the interface between the two parts dominates over the bulk resistivity of the metal. [31]

Resistance at contacting faces occurs largely due to the microscopic roughness of nominally flat surfaces. This results in constriction of the current through the small area of the contacting asperities. [14]

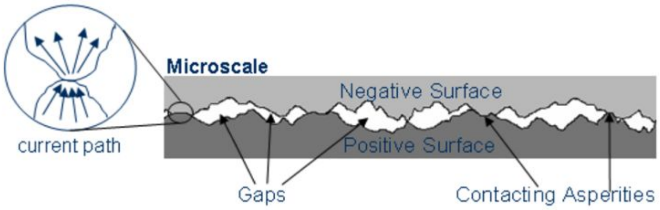

Figure 7-1: Actual contact area restricts current flow through asperities. [37]

Greenwood and Williamson found that the actual area of contact is roughly proportional with applied load and, to good approximation, independent of nominal area of contact. Furthermore, the actual area of contact depends almost exclusively on the normal force applied to the contact and the hardness of the softer material.[31] That is to say,

$$A_c = \frac{F}{H} \tag{7.1}$$

This result is quite nonintuitive and has significant implications in the design of low resistance press-fit electrical connections and suggests one of the most important requirements is to preload the joints.

Reliable press-fit electrical connections exist and have been used (especially in the telecom and industrial markets). [20] However, they largely rely on producing cold-welded gas tight connection zones whereby the contact faces are plasticly deformed to increase the actual contact area. These connections are permanent and may not be re-used. [29]

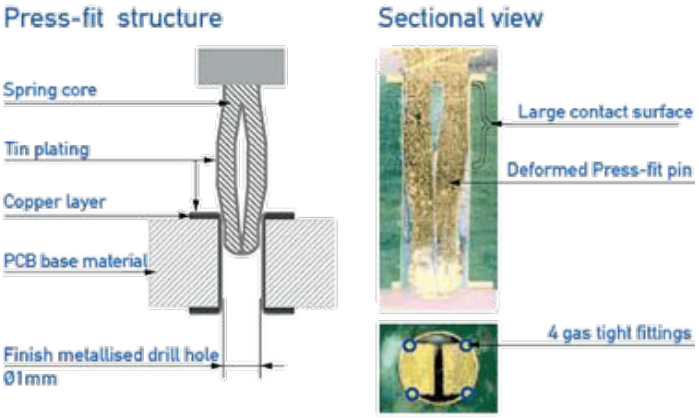
Press-fit structure
Sectional view
Spring core
Tin plating
Copper layer
PCB base material
Finish metallised drill hole
Ø1mm
Large contact surface
Deformed Press-fit pin
4 gas tight fittings

Figure 7-2: Industrial Press-Fit Connection [18]

7.2 Reversibility

In order for the parts to be considered reversible, they must be able to be joined and unjoined multiple times without a significant effect on the resistance of the joint.

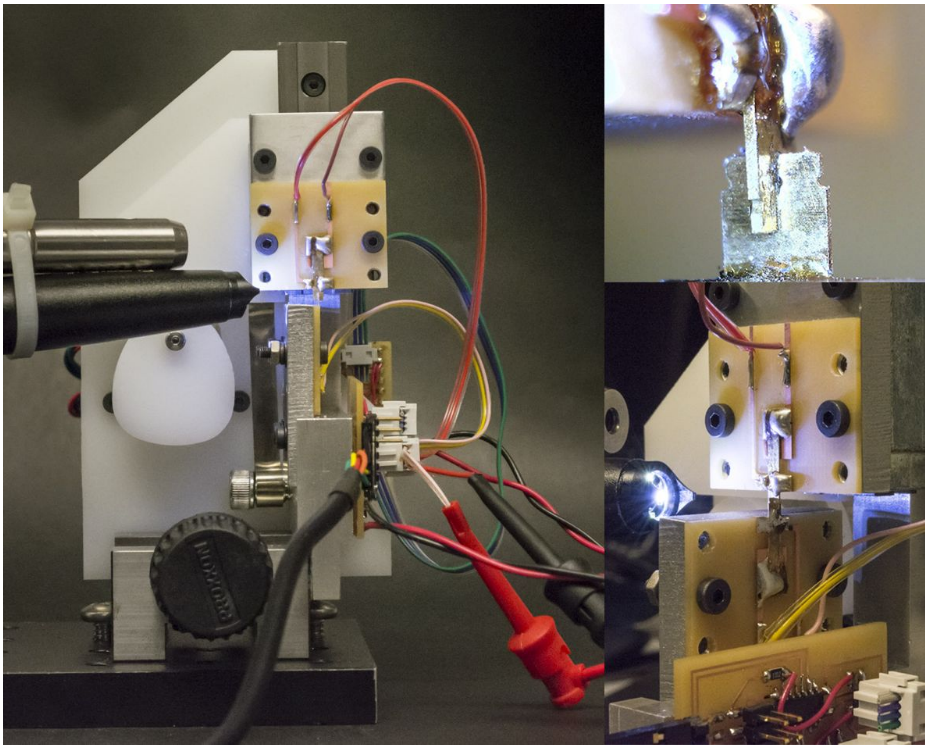

Figure 7-3: Joint cycling machine

To measure this, I developed an automated joint cycling machine. A stepper motor drives a cam which moves a test specimen up and down, attaching and detaching it from another test specimen. A 3 N constant force spring applies a repeatable load on the joint during measurement. The resistance of the joint is measured using a four-wire resistance measurement circuit as pictured in Figure 7-4. Current is applied via two terminals while voltage is measured on another two. In this case, 1 A of current is sourced through the joint by a benchtop power supply operating in constant current mode. The voltage difference (in mV) can then be directly measured by a benchtop multimeter and translated into a reading of resistance (in mΩ). The measurement is synced with the rest of the mechanism through a python script that polls the multimeter through a GPIB interface whenever the joint is connected.

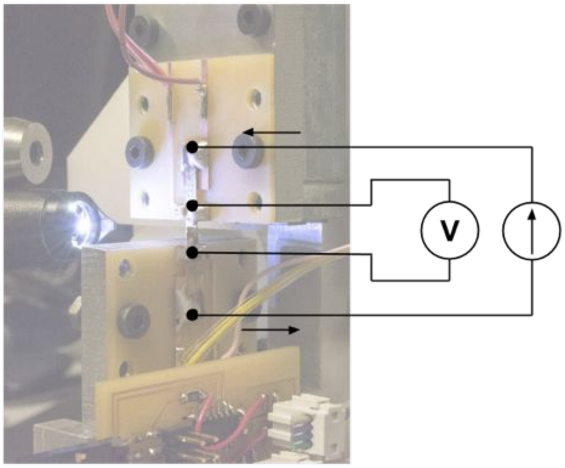

Figure 7-4: Joint cycling machine

The data (Figure 7-5) shows that the resistance settles to a constant value ($\approx 1\,\text{m}\Omega$) after 250 cycles. While it is possible the high initial peak of 7.5 mΩ is due to the cycling machine settling in, the overall decrease in resistance over the first 250 cycles is likely indicative of a scraping contact as the parts are joined and unjoined. The scraping causes plastic deformation of the asperities on the contacting surfaces and increases the effective contact area, thereby increasing the effective conductance of the joint.

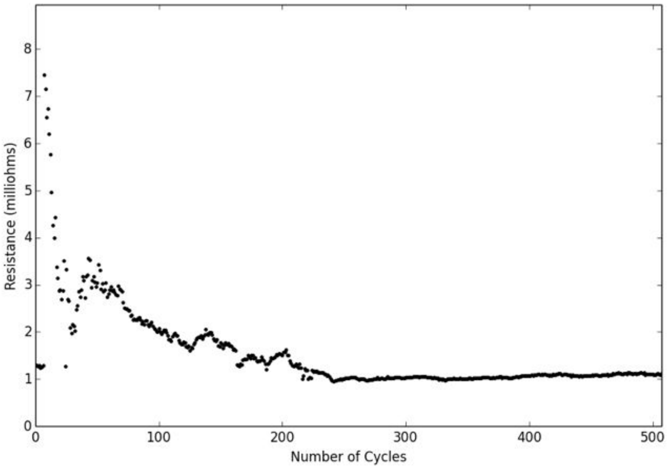

Figure 7-5: Resistance of joint vs number of cycles

7.3 Response to Load of a Single Joint

It is also interesting to examine how the contact resistance of a joint changes with applied load. The same four-wire resistance measurement technique and fixture that was used to test the repeatability of the joints can be used in the Instron to test the response of a single joint to applied compressive load.

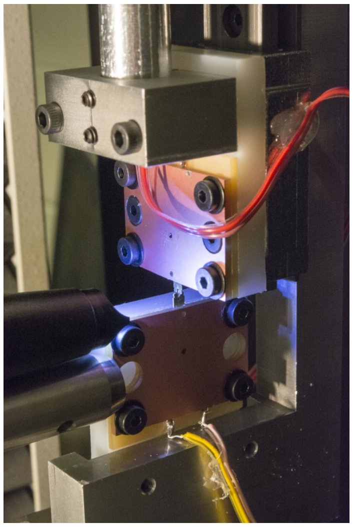

Figure 7-6: Instron measurement test setup

Figure 7-7(a) shows the resistance and load required during the press-fit assembly of a single joint. It is clear, here, that the instantaneous force required to press-fit the parts together is directly proportional to the conductance of the joint. This makes sense given our understanding that actual contact area is directly proportional to applied normal force. It is worth noting that the loads shown here are an order of magnitude greater than the joint cycling test needed to insert and remove a part. I believe this is in large part due to a lack of compliance in the Instron fixturing. In contrast with the joint cycling machine, there is no play to allow the joint to self-align.

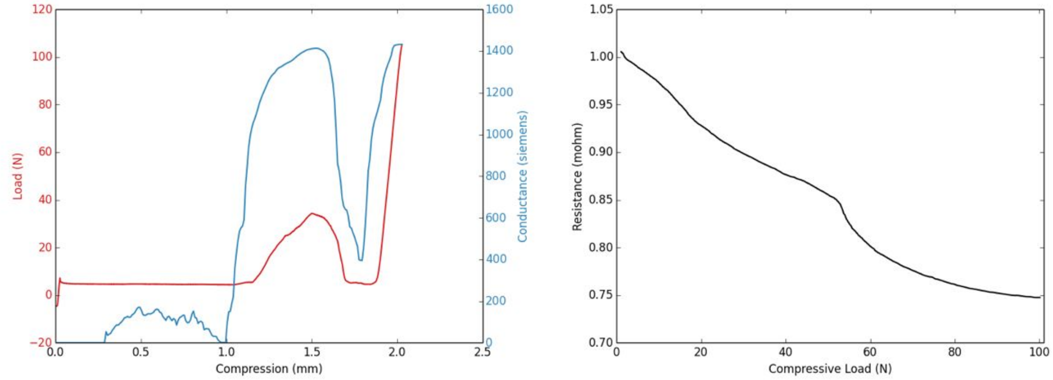

Figure 7-7: Conductance and load vs displacement (left). Resistance of joint with applied compressive load (right).

To understand how the compressive pre-load of a joint influences its resistance, we can look more carefully at the last 250 µm of extension in 7-7(b).

Plotting the resistance of the joint with respect to applied load (Figure 7-7(b) shows a roughly linear relationship for less than 50N and then a square-root relationship for above 50N. This is consistent with theory, which says that the contact conductance should be roughly proportional to the square root of the applied load, and shows that increasing the preload of the structure (and therefore the joints) results in a desirable decrease in contact resistance. Beyond 100N of compressive load, I found that the test specimens buckled and plastically deformed.

7.4 Bulk Response to Load

While modeling and measuring the performance of individual joints is important, it is perhaps more so important to model and measure how the joints work together as a bulk solid.

To determine how the individual joints perform as a solid, I constructed a block made entirely of brass parts and subjected the structure to various loads in the Instron to see how the conductance of the solid varies with applied load. The specimen, pictured in Figure 7-8, is 10 pitches wide and long (roughly 0.5 inches) and three parts tall (roughly 0.375 inches).

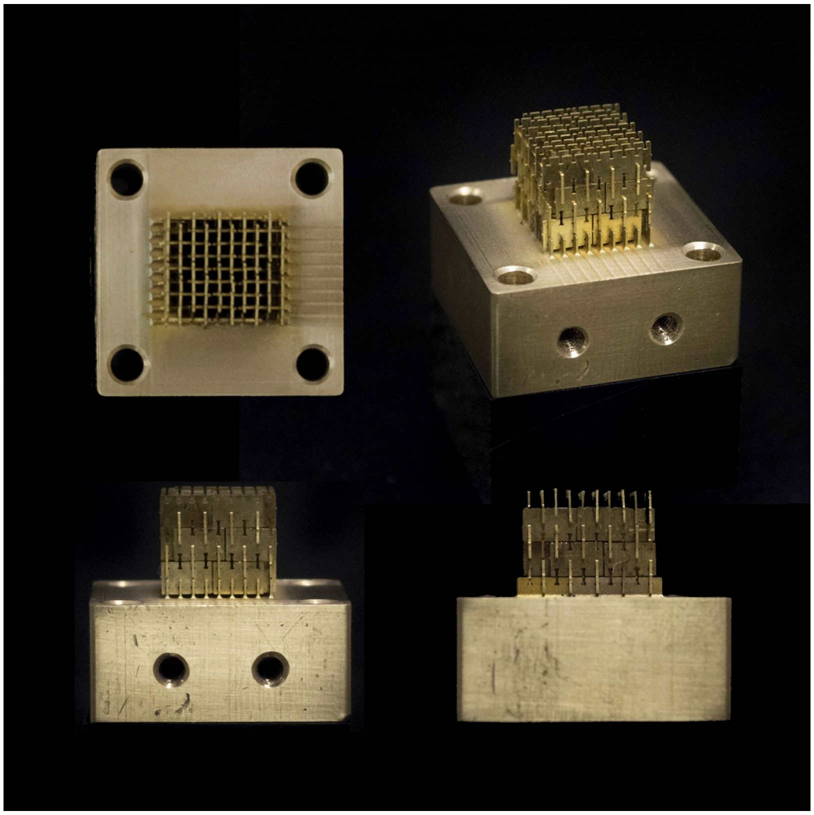

Figure 7-8: Bulk resistance test specimen.

The test specimen was held on the top and bottom by brass fixture blocks with press-fit slots. The fixture blocks were made using the wire-EDM by cutting brass bar-stock with two profiles at 90-degrees to each other (Figure 7-9). A four-wire resistance measurement was made using four ring terminal connections to the two brass fixture blocks. A delrin fixture block electrically isolated the test specimen from the Instron and provided for an area that could be gripped by the Instron clamps (Figure 7-10).

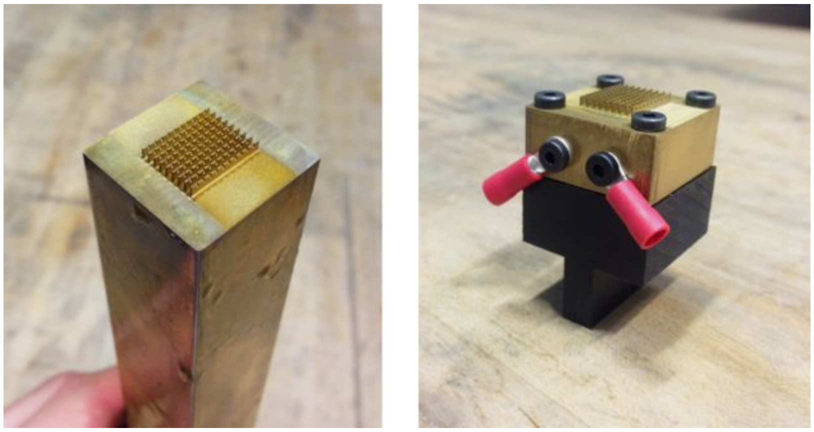

Figure 7-9: Bulk resistance fixture block.

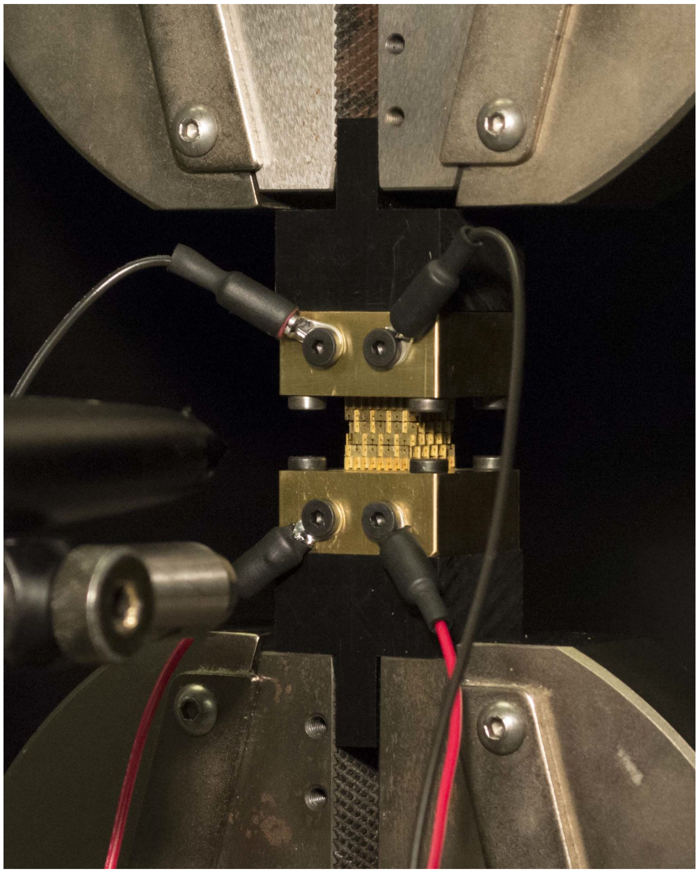

Figure 7-10: Bulk resistance test specimen in instron.

I used the Instron to cycle compressive loads ranging from 5N up to 40N and found that the conductance of the bulk specimen increased with each cycle (Figure 7-11. As increasing load was applied, the conductance increased; as the applied load was reduced, the conductance decreased but at a rate far less than it had previously increased with. This resulted in an irreversible increase in conductance with each cycle.

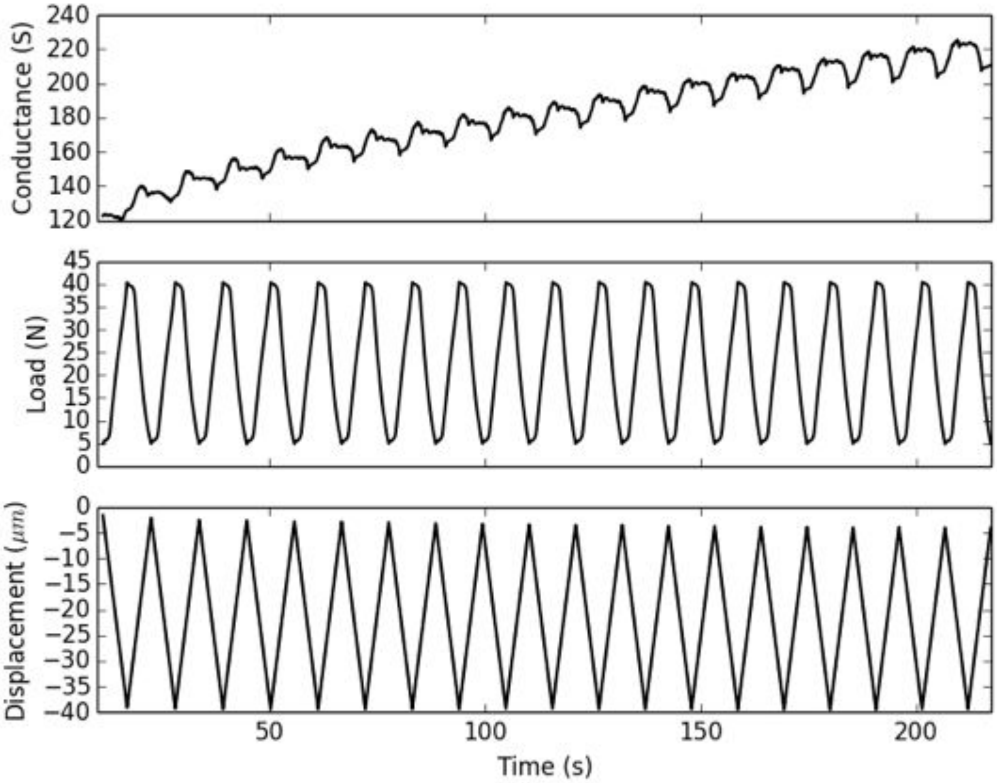

Figure 7-11: Time series of conductance, load, and displacement over 20 cycles.

The data can be plotted independently of time to see the hysteresis cycle and visualize the conductance as a function of displacement (Figure 7-12)

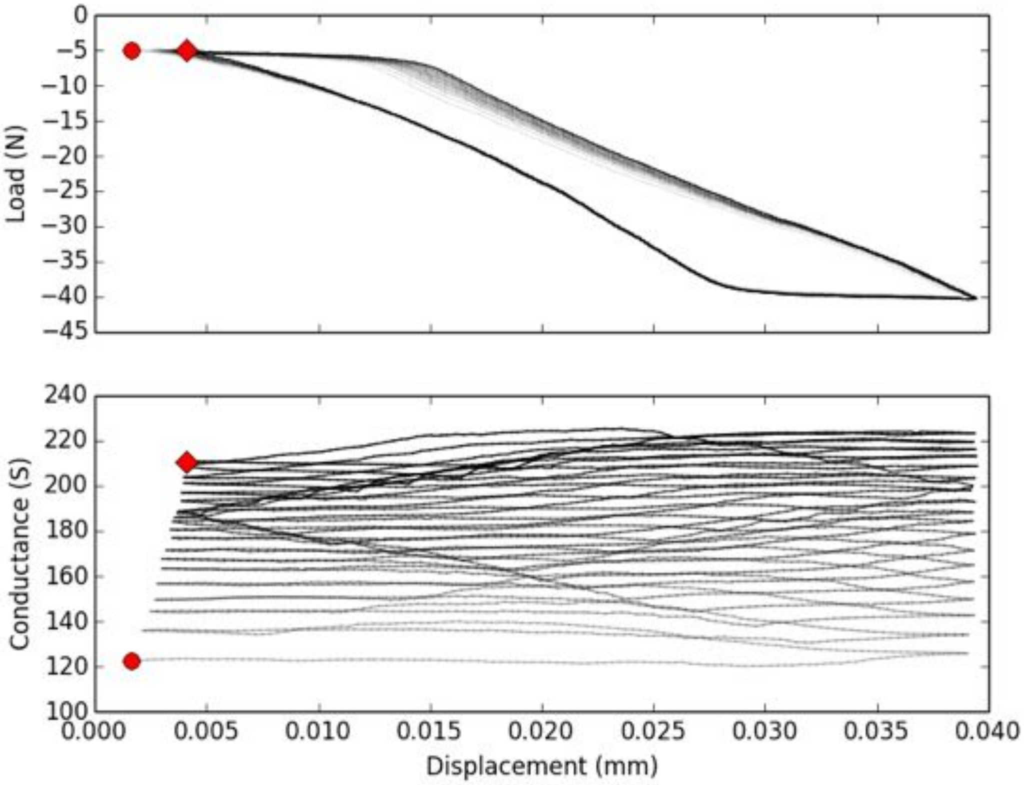

Figure 7-12: Plot of conductance/extension and load/extension loops over 20 cycles. The red circle denotes the start of the experiment and the red diagonal denotes the end.

The load/extension cycle showed no appreciable change over the course of 20 cycles on the side of decreasing load. On the other hand, the side of increasing load moved approximately 2 µm, which suggests a flattening of micro-scale peaks. That is to say, the Instron needed to move an additional 2 µm to apply the same 5 N of force on the 20th cycle as it did on the first cycle. This trend can be seen even more clearly by looking at the change in extension needed to produce 5 N of force over each cycle and the resulting change in conductance due to the flattening of micro-peaks and increase of actual contact area (Figure 7-13).

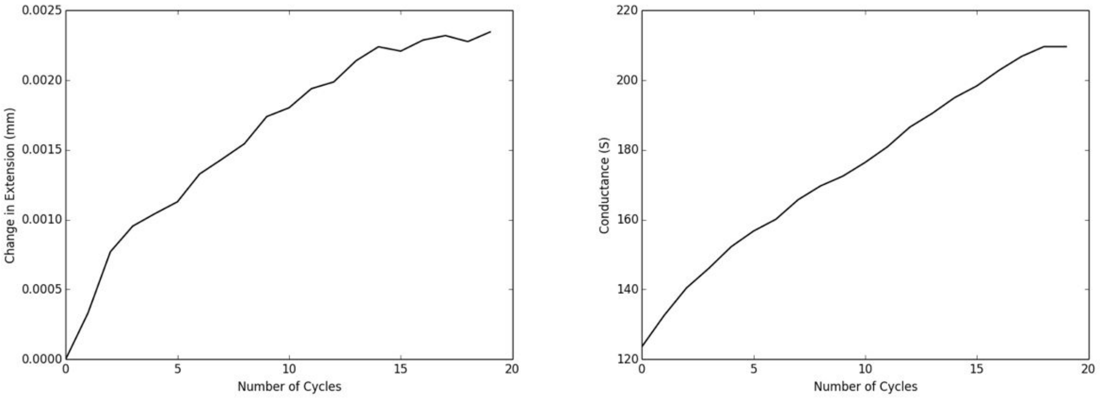

Figure 7-13: Plot of change in extension and conductance over 20 cycles.

7.5 Bulk Temperature Dependence

It is often important to test electronic connections at elevated temperatures to ensure reliable operation.

In order to test the performance of these electronic digital material assemblies at elevated temperatures, I installed a resistive cartridge heating element and temperature sensors in the brass fixture block.

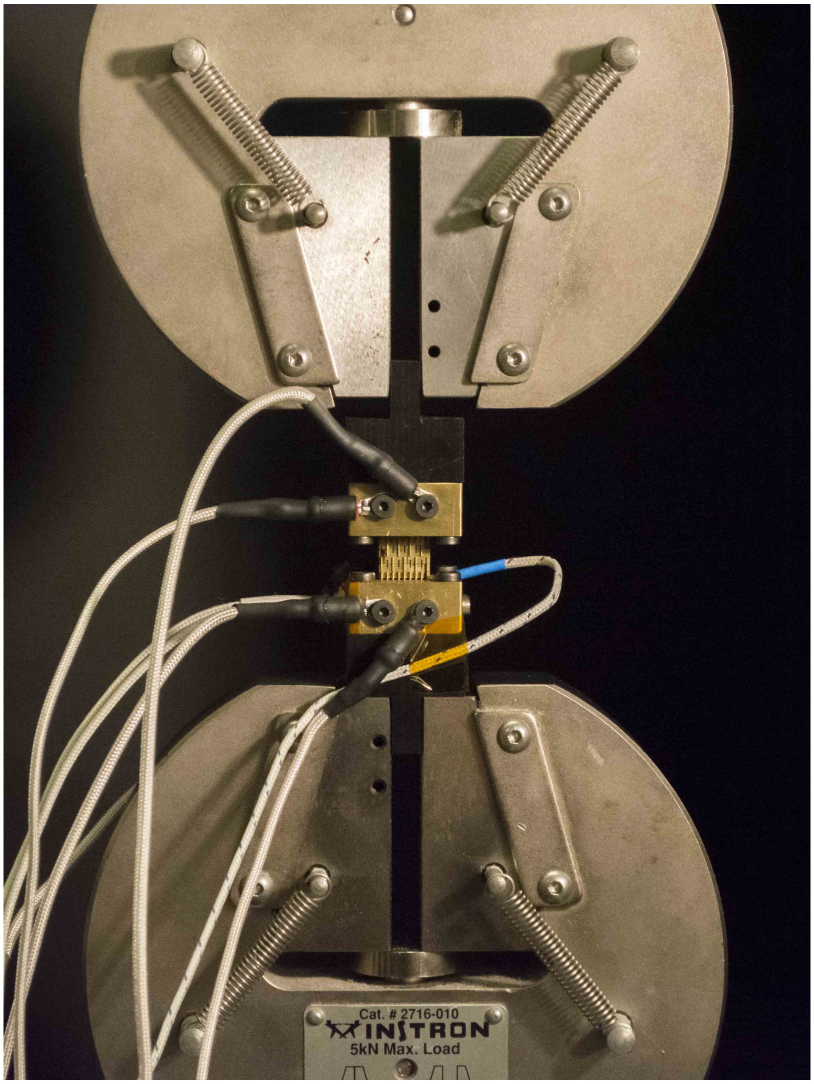

Figure 7-14: Temperature response fixture

The 12V 40W cartridge was operated at 10V from a lab power supply. A 10K thermistor, connected through a Teensy 3.1 microcontroller, was used to gather online temperature data while the test was running. A type K thermocouple connected to an Extech portable multimeter served as a way to ensure the thermistor was calibrated and operating correctly. A fan was used to cool the device more quickly.

The test specimen and fixture were installed into the Instron. The Instron served two purposes: to apply a known compressive load to the device under test and to serve as a sensor for thermal expansion effects.

I cycled the temperature of the device from room temperature (24 °C) up to 80 °C four times and measured conductance and compressive load applied due to thermal expansion. Figure 7-15 shows the time series data from this experiment.

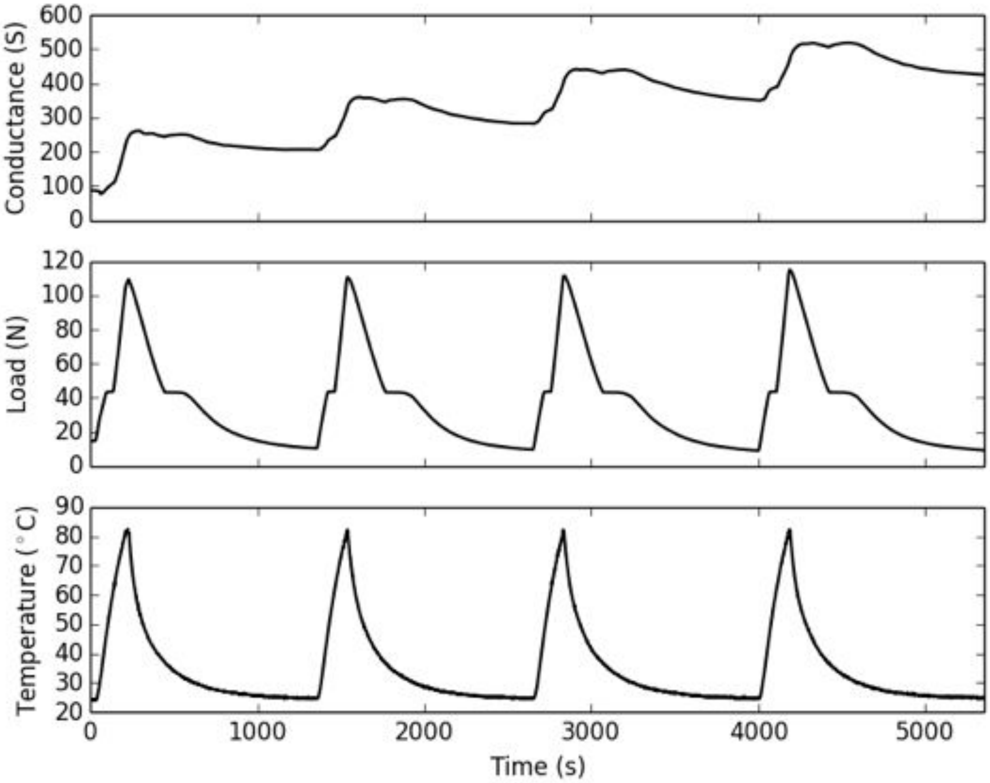

Figure 7-15: Time series showing conductance, load, and temperature over four cycles.

I found that temperature cycling had much the same effect as load cycling. Each increase in temperature resulted in a significant increase in conductance. Once the heater is switched off, the conductance decreases gradually but less so than it had increased previously with the applied heat. The result is an irreversible increase in conductance with each thermal cycle.

This result can be attributed, in large part, to the thermal expansion of the solid and the resulting applied compressive load. I used the Instron to measure this applied load on the device and fixture, which can be seen in Figure 7-16. The data shows a completely reversible increase in load with increased temperature. In other words, cycling the temperature of the device creates a reversible load cycle which acts in the same manner described in the previous section to increase conductance irreversibly.

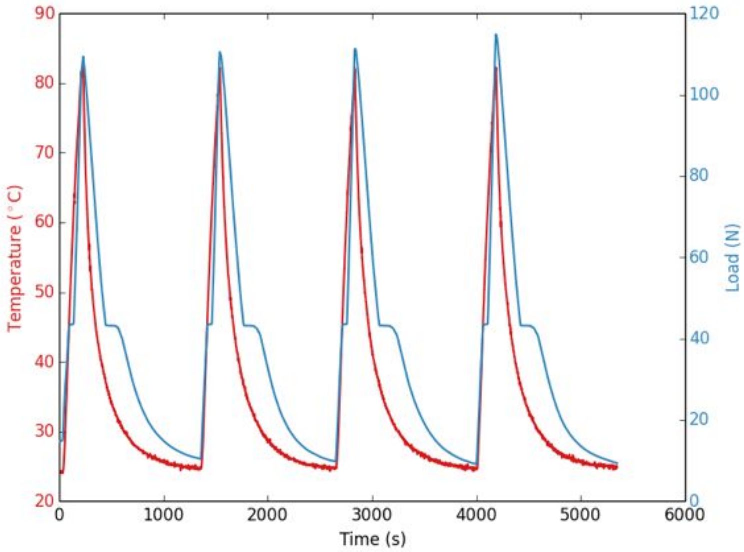

Figure 7-16: Plot of conductance over four temperature cycles.

The data includes artifacts at 43 N which I believe are a result of the fixture clamps slipping. This was validated by re-fixturing the part, applying different initial loading conditions, and finding the same artifact at precisely 43 N.

The increase in conductance due to the loading from thermal expansion far outweighs the increase in bulk resistivity due to the increased temperature. Metals typically have a positive temperature coefficient of resistance (α) that is approximately $3e^{-3}/K$. The increase in resistance of a metal due to an increase in temperature can therefore be expressed by the equation

$$R = R_0(1 + \alpha \Delta T)$$

Therefore, for 1.5 mΩ resistance, a 60K increase in temperature would result in a resistance increase of 0.27 mΩ. This is an order of magnitude less than the decrease in resistance due to an an 80 N applied load ($\approx$ 2 mΩ).

7.6 Surface Roughness of Contacting Surfaces

Given the importance of surface roughness (or lack thereof) in creating good electrical contacts, it is informative to look closely at the microstructure of the contacting surfaces of the parts.

To do this, I used a scanning electron microscope to compare the surface of a used and unused part.

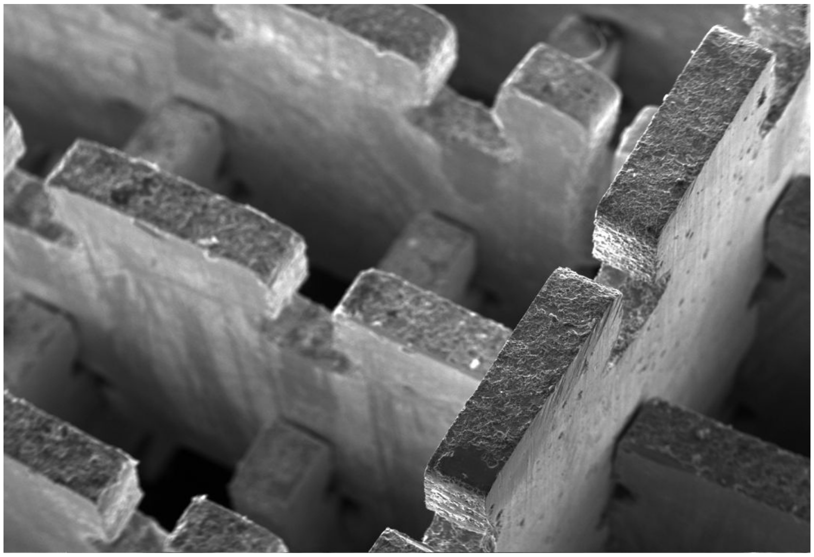

Figure 7-17: SEM micrograph of a part in an assembly.

Figure 7-18 shows a micrograph of a slot that has not been used and Figure 7-19 shows a slot that has been load cycled. When looked at under this magnification it becomes clear that the nominal area of contact has little to do with the actual area of contact. In comparing the two slots, evidence of micro-peak flattening can be seen on the vertical face in Figure 7-19 (on the left) and in the darkening on the bottom face of the slot from the edge of the contacting part.

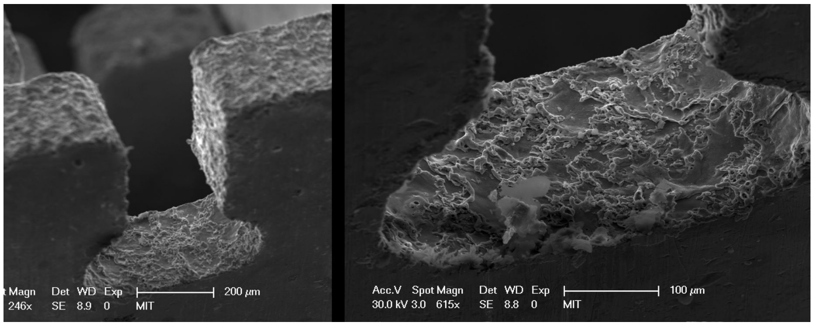
t Magn Det WD Exp 200 µm
246x SE 8.9 0 MIT
Acc.V Spot Magn Det WD Exp 100 µm
30.0 kV 3.0 615x SE 8.8 0 MIT

Figure 7-18: SEM micrograph of a slot that has not been used.

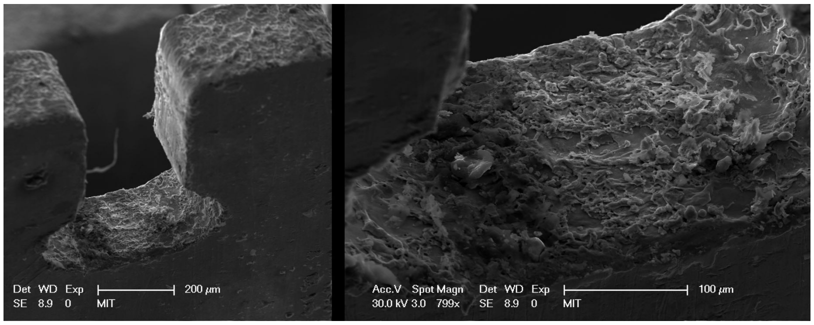
Det WD Exp 200 µm
SE 8.9 0 MIT
Acc.V Spot Magn Det WD Exp 100 µm
30.0 kV 3.0 799x SE 8.9 0 MIT

Figure 7-19: SEM micrograph of a slot that has been used.

7.7 Implications for Reducing Contact Resistance

Given these results, there are a number of implications for improving upon the current techniques for discretely assembling electronic interconnections.

As we saw in Section 7.1, the equation for actual area of contact depends solely on the normal force applied to the contact and the hardness of the softer material. This leads to the conclusion that we can improve the performance of the joints by increasing the amount of preload on the joint and by using a softer metal.

The load cycling of the bulk solid (Figure 7-11) demonstrated the performance of a discretely assembled structure with 22.5 N of preload. The results suggest that increasing this preload would reduce the effects of repeated load cycles on the bulk conductance.

It is common for mechanical electrical contacts to utlize a thin plating of a soft metal (like gold or tin) to improve contact conductance. The plating is designed such that the micro-peaks on the contacting surface plastically deform during assembly when there is sliding or wiping contact. The thickness of this plating can be specified to last for a number of cycles of joining and unjoining the parts. [31]

In the interest of maintaining a single material per part-type, it may be possible to utilize flexural contacts like those described in Section 2.1.2 to improve electrical contact rather than using a soft metal plating.

Another possible technique to improve electrical contact between parts would be to do the opposite of plating: electro-polishing. This process would significantly reduce the surface roughness and improve the effective area of contact between parts by eroding the largest micro-peaks. This technique may also be applied to silicon parts (albeit with different chemical treatments).

Chapter 8

Scaling

In order to compete with conventional microelectronic fabrication methods, the parts will need to be scaled down significantly. Doing so will require finding efficient ways of making vast numbers of very small parts.

8.0.1 Part Fabrication

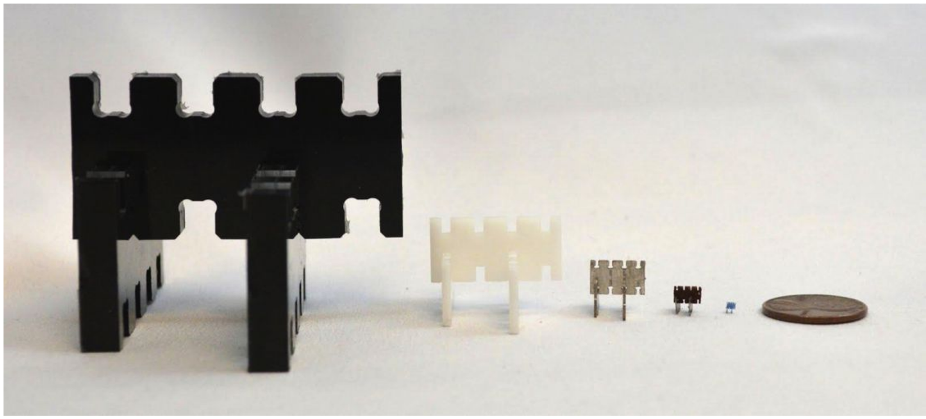

Figure 8-1: A number of parts made at various scales with feature sizes ranging from 0.25 inches to 100 µm

The assemblies presented in this work have a lattice pitch that is the same as the pin spacing on SOIC surface mount components. Part fabrication can be scaled down to feature sizes of 100 µm (a demagnification of 2.5x) to achieve QFN-pitch lattices with similar tools to those used in this work. Figure 8-2 shows a QFN-pitch steel part made with the wire-edm with a 0.002 in wire (producing a roughly 75 µm kerf). It also shows a similar QFN pitch plastic part made via excimer micromachining.

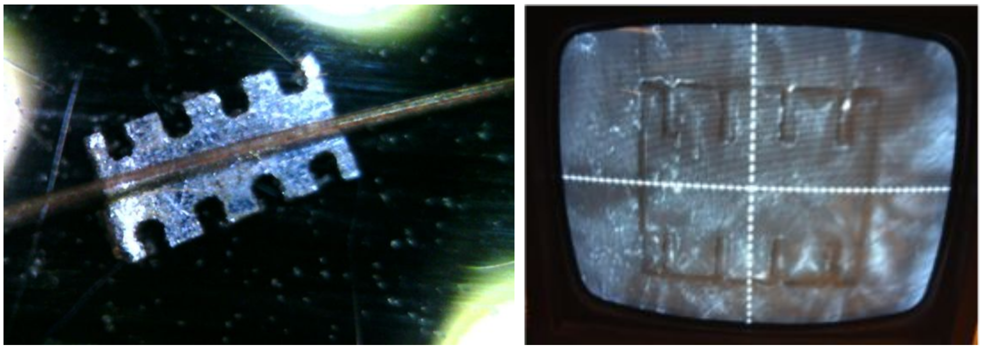
(a) Wire-EDM micro-part (b) Excimer micro-part

Figure 8-2: A QFN pitch part made via wire-edm shown with a human hair for scale (left). Another QFN pitch part made via excimer laser micromachining (right).

Diode-pumped solid-state laser micromachining can achieve feature sizes of approximately 15 µm. This fabrication method is relatively slow, however, and would not be capable of producing parts at that scale fast enough. An excimer laser, on the other hand, can use mask projection to create whole parts at a time and should be capable of producing parts with a little less than 10 µm feature sizes.

To scale down beyond this, the best option is likely deep reactive ion etching, with which sub-micron (down to tens of nanometer) feature sizes can be created. This method would also allow whole wafers to be processed at once, producing upwards of 350 thousand parts at once (assuming 1 µm feature size parts made from a 100 mm diameter wafer).

8.0.2 Capacitors

We can look at the scaling of capacitors to get a rough sense of how electronic functionality scales with length-scale and number of parts in an assembly.

From Section 4.1.1 we can use Equation 4.4 ($C = 10\epsilon n p$) to get a rough indication of how many parts are needed to assemble various amounts of capacitance at a given length-scale.

For example, for a lattice pitch of 1.27 mm (0.05 inches):

- 1 µF requires on the order of 5 million parts.
- 1 nF requires on the order of 5 thousand parts.
- 1 pF requires on the order of 5 parts.

Furthermore, we can now compare the space efficiency (capacitance per volume) of a discretely assembled capacitor to one used commercially. Figure 8-3 shows how the capacitance per volume scales with the characteristic length of the discrete lattice and compares it to a conventional 1 µF 1206 surface mount capacitor.

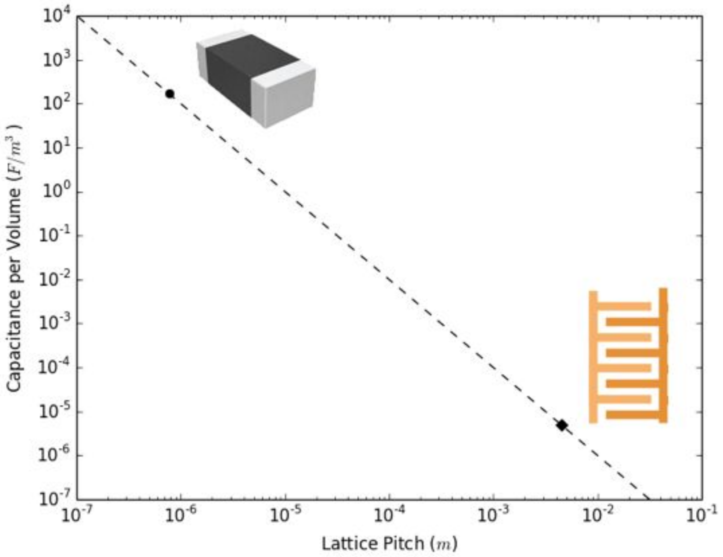

Figure 8-3: A plot showing how capacitance per volume increases with decreasing lattice pitch.

What the plot reveals is that, in order to match current capacitor densities, the lattice pitch needs to be a little less than one micron. Of course, this neglects possible modifications to increase capacitance like adding a dielectric substance to fill the negative space in the lattice.

8.0.3 Integrated Circuits

The Intel 4004, the first commercially available microprocessor, contained roughly 2,300 transistors. [23] It is clear, then, that even the simplest digitally assembled microprocessor will contain many thousands of discrete parts.

Current microprocessors contain upwards of a few billion transistors in an area less than $400\,\mathrm{mm}^2$ (or about 10 million transistors per square millimeter). Assuming a discretely assembled transistor looks approximately like the schematic render depicted in Figure 5-2, each transistor would be composed of roughly 14 discrete parts. This implies part densities upwards of 100 million parts per square millimeter, and furthermore, necessitates parts that are $2\,\mathrm{nm}$ in size.

While it is very unlikely a discretely assembled transistor that is this small will look exactly like Figure 5-2, these numbers give a good indication of how this fabrication strategy scales.

Chapter 9

Assemblers

It is clear that in order to achieve assemblies of the magnitude and complexity as was discussed in the previous chapter, automated assembly will be necessary. This is further illustrated by looking at the scaling of the required part placement rate in order to achieve a volumetric build rate of one cubic-inch in ten minutes at ever decreasing scales.

Characteristic part size	Density (parts/$in.^2$)	Deposition rate (parts/sec)
5 mm	10^2	10^0
2 mm	6×10^2	10^1
20 µm	6×10^6	10^5

Table 9.1: Table showing how part deposition rate scales with characteristic part size.

The table shows that with 20 µm parts, the required deposition rate is ultrasonic. Inkjet printers deposit ink at roughly kilohertz frequencies and represent a possible upper-limit of part-placement speed. To achieve deposition rates beyond this, requires parallelization.

This parallelization can be realized in various ways. In one implementation (discussed in Section 9.1.1), whole layers of an assembly may be placed at once. Another way to achieve parallelization is through the use of multiple serial-assemblers. This kind of implementation is discussed in Section 9.1.2.

9.1 Discrete Relative-Motion Assemblers

Assemblers will look and function differently than 3D printers and other rapid fabrication tools since the assembler should be able to take advantage of the inherent traits of digital material structures. Positioning can be done relative to the digital material lattice, thereby offloading the job of precise positioning to the structure rather than the assembler. This means the assembler only needs to be able to move from one lattice location to the next and any errors within the tolerance of the press-fit will be corrected as it goes.

9.1.1 Parallel assembly

Parallel assembly of whole layers of an object at once is one foreseeable way to scale assembly speed. One such implementation of this involves an array of pins in which parts are loaded sequentially into the grid from one edge. Rows may either be loaded sequentially, one after the other, or in parallel, further increasing the speed at which parts can be placed.

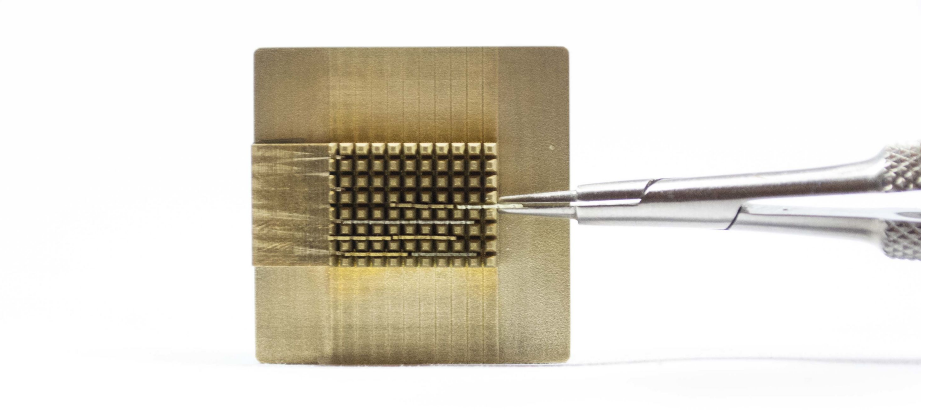

Figure 9-1: Parts are sequentially loaded into the rows of the pin array from the edge.

Once all of the parts for the layer are loaded, the pins are brought into alignment with the uppermost layer of the structure being built. The pins align with the negative space in the top-most layers. As the pin array and the structure are brought together, the parts in the pin array press-fit into the structure.

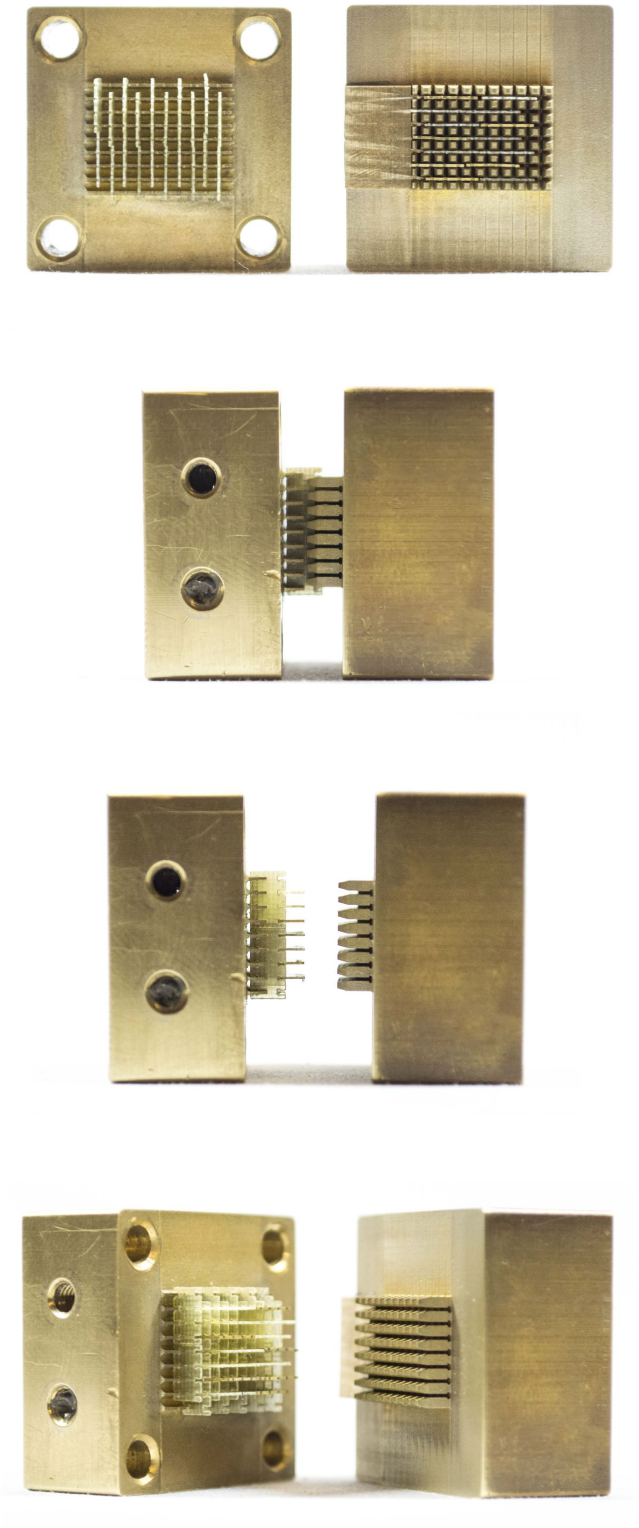

Figure 9-2: Experimental demonstration of parallel assembly technique.

While this technique is capable of placing whole layers of the structure at a time, it is also prone to errors. Figure 9-3 shows two failure modes of the parallel assembly strategy in which some parts are not deposited correctly and some parts from the structure are inadvertently removed.

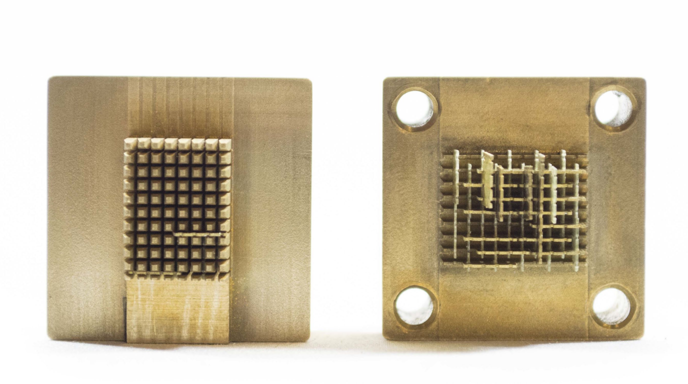

Figure 9-3: Failure modes of the parallel assembly technique.

9.1.2 Serial assembly

While serial assembly is limited to roughly kilohertz part deposition rates, by using multiple serial assemblers in parallel, assembly speeds can be scaled to enable the construction of dense assemblies from small parts.

Figure 9-4 illustrates one such instantiation of an assembly strategy whereby a stapler-like tool-head stores and places parts in the lattice below. As the tool-head is activated, the stapler head registers to the lattice with alignment features and deposits a part.

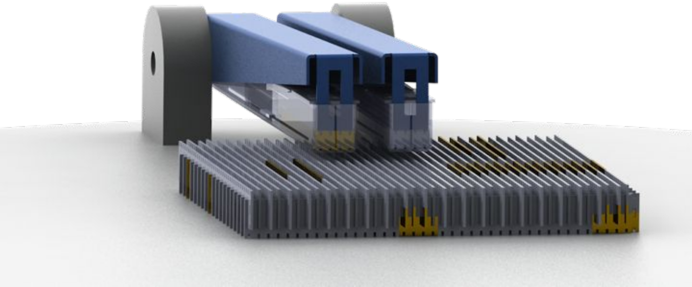

Figure 9-4: A render of a stapler assembler.

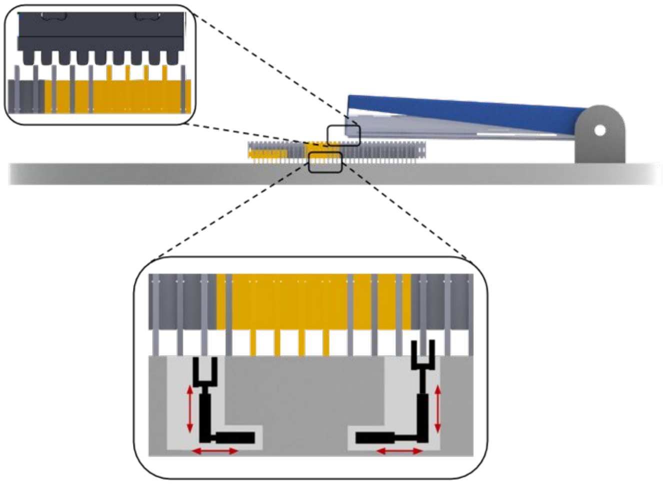

Figure 9-5: A diagram showing the parts of a stapler assembler.

The lattice below may be moved using a conventional motion system or by a discrete motion system like the one shown in Figure 9-5 and Figure 9-6. In this case, the discrete motion system works using a mechanism that converts continuous rotation of a shaft into discrete steps.

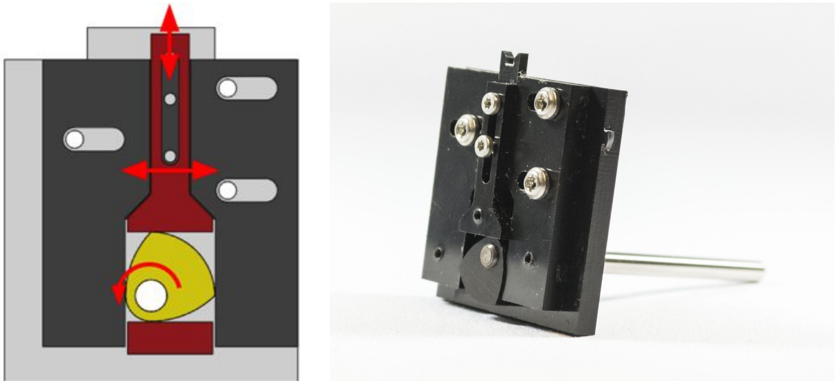

Figure 9-6: Rotary cam mechanism to produce discrete steps from continuous rotation.

Figure 9-7 shows a prototype of a stapler-style assembler I developed with Steven Gerasimoff. The assembler features alignment pins that register to the lattice so that a part is deposited in the correct position and orientation. This alignment mechanism can be seen being used in Figure 9-8.

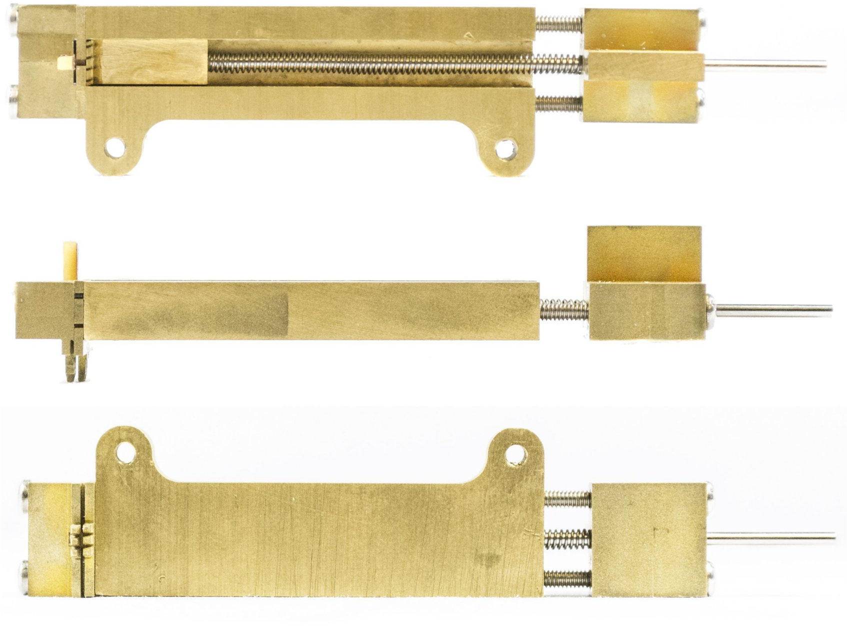

Figure 9-7: A prototype of a stapler-style assembler.

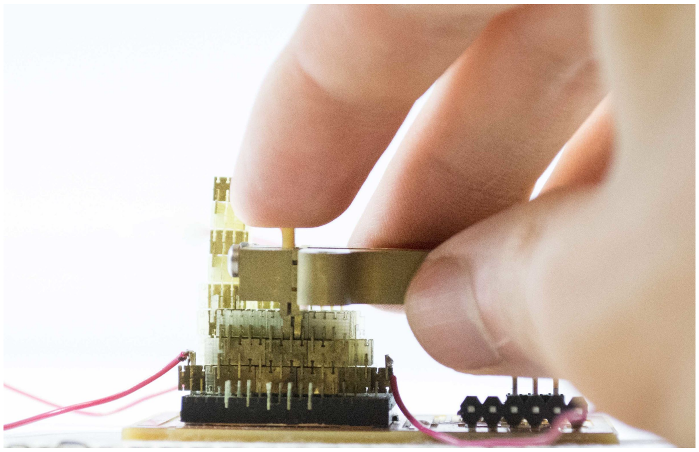

Figure 9-8: The stapler assembler in use.

Chapter 10

Conclusion

I have shown that it is possible to discretely and reversibly assemble most of the primary functions of micro-electronics from less than ten unique part-types.

The press-fit joints between parts have been shown to be adequate to enable the assembly of components of similar quality to current surface mount chip technologies. I have also identified a number of ways to improve the performance of these electronic assemblies, which include adding a soft-metal plating to the conductive part-types, using pre-loaded flexural contacts, or electro-polishing to reduce contact resistance between parts.

Discretely assembly of active electronic components may require an alternative assembly strategy to the press-fit connection scheme. For example, semiconducting parts could be assembled in a planar stack and then press-fit into the lattice through metal components.

In order to compete with existing technologies, electronic digital materials will need to undergo a series of shrinks to reach scales where the lattice pitch is on the order of a micron. It is within the capability of current micro and nano-fabrication tools to build the parts and tools needed to accomplish this.

The clear next step is determining robust methods of quickly assembling vast numbers of these parts.

Bibliography

[1] Oxford Lasers Micromachining and Measurement. http://www.oxfordlasers.com/.

[2] Schottky Diode Procedure. Technical report, Center for Nanoscale Chemical Electrical Mechanical Manufacturing Systems.

[3] Resistor Construction. http://www.learnabout-electronics.org/resistors_08.php, 2013.

[4] Engineering ToolBox. www.engineeringtoolbox.com, 2014.

[5] MatWeb. www.matweb.com, 2014.

[6] Jacques Audet. Q Factor Measurements on L-C Circuits. *QEX*, (February):7–11, 2012.

[7] Boedecker. Anti-Static and Conductive Plastics. www.boedeker.com/esdmatls.html, 2013.

[8] Hu Chenming. MOS Transistor. In *Modern Semiconductor Devices for Integrated Circuits*, chapter 6, pages 195–258. Prentice Hall, Upper Saddle River, 2010.

[9] Rick Cory. Schottky Diodes. *Microwave Product Digest*, (February):1–5, 2009.

[10] Gregory Allan Crawford. *Process Characterization of Electrical Discharge Machining of Highly Doped Silicon.* Masters of mechanical engineering, Massachusetts Institute of Technology, 2012.

[11] Dayton Progress Corporation. Stamping Basics Fundamentals & Terminology. Technical report, Dayton Progress Corporation, 2003.

[12] Piet Van Dijk. Critical Aspects of Electrical Connector Contacts.

[13] Corey M Dunsky. Laser material processing in microelectronics manufacturing : status and near-term opportunities. Technical report, Coherent, Inc.

[14] J. a. Greenwood and J. B. P. Williamson. Contact of Nominally Flat Surfaces. *Proceedings of the Royal Society A: Mathematical, Physical and Engineering Sciences*, 295(1442):300–319, December 1966.

[15] Jonathan Hiller and Hod Lipson. Methods of Parallel Voxel Manipulation for 3D Digital Printing. In *Proceedings of the 18th solid freeform fabrication symposium.*, page 12, 2007.

[16] Jonathan Hiller and Hod Lipson. Design and analysis of digital materials for physical 3D voxel printing. *Rapid Prototyping Journal*, 15(2):137–149, 2009.

[17] Matthew a. Hopcroft, William D. Nix, and Thomas W. Kenny. What is the Young's Modulus of Silicon? *Journal of Microelectromechanical Systems*, 19(2):229–238, April 2010.

[18] IMS Connector Systems. PCB Mounted Connectors. http://www.imscs.com/pcb-mounted-connectors.html.

[19] Robert H Johns. Homebrew Your Own Inductors. *ARRL Handbook*, page 35, 1997.

[20] Joseph Lynch. Adapting Press-Fit Connection Technology for Electronic Modules Harsh Environments. Technical Report Idc.

[21] Brett Lyons, John Ochsendorf, and Eric C Leuthardt. Frontiers of engineering. *The Bridge*, 42(1), 2012.

[22] R. MacCurdy, a. McNicoll, and H. Lipson. Bitblox: Printable digital materials for electromechanical machines. *The International Journal of Robotics Research*, July 2014.

[23] Scott Mueller. Pre PC Microprocessor History Microprocessors from 1971 to the Present. 2006.

[24] Igor Novák and Igor Krupa. Electro-conductive resins filled with graphite for casting applications. *European Polymer Journal*, 40(7):1417–1422, July 2004.

[25] OMAX. OMAX MicroMAX JetMachining. http://www.omax.com/waterjet-cutting/machine/model/MICROMAX, 2014.

[26] George A Popescu, Tushar Mahale, and Neil A Gershenfeld. Digital materials for digital printing. *NIP & Digital Fabrication ...*, pages 1–4, 2006.

[27] Horace Pops. The Metallurgy of Copper Wire. Technical report, HSM Wire International.

[28] Paul G. Slade. *Electrical Contacts: Principles and Applications, Second Edition.* CRC Press, 2013.

[29] T Stolze, M Thoben, M Koch, and R Severin. Reliability of PressFIT connections. Technical report, Infineon Technologies AG, Warstein.

[30] Dennis M Sullivan. *Electromagnetic Simulation Using the FDTD Method [Hardcover].* Wiley-IEEE Press; 1 edition, 2000.

[31] Roland S Timsit. Electrical Contact Resistance: Fundamental Principles. In Paul G. Slade, editor, *Electrical Contacts*, pages 3–111. 2014.

[32] Vishay. Precision Thin Film Technology. Technical report.

[33] Vorarlberg University of Applied Sciences. Dry Etching. http://www.fhv.at/fhv-science/microtechnology/dry-etching-rie-and-drie, 2014.

[34] Jonathan Ward. *Additive assembly of digital materials*. Master of science in media arts and sciences, Massachusetts Institute of Technology, 2010.

[35] Christopher Wargo. Characterization of Conductors for Printed Electronics. Technical report, PChem Associates, Bensalem, PA.

[36] Feng Tsai Weng, Chen Siang Hsu, and Wen Feng Lin. Fabrication of Micro Components to Silicon Wafer Using EDM Process. *Materials Science Forum*, 505-507:217–222, 2006.

[37] W Everett Wilson, Santosh V Angadi, and Robert L Jackson. Electrical Contact Resistance Considering Multi-Scale Roughness. In *Electrical Contacts*, pages 190–197, 2008.

[38] Woodbank Communications Ltd. Battery and Energy Technologies. http://www.mpoweruk.com/semiconductors.htm, 2005.